

Mitigating Staleness in Asynchronous Pipeline Parallelism via Basis Rotation

Hyunji Jung ^{*1} Sungbin Shin ^{*1} Namhoon Lee ¹

Abstract

Asynchronous pipeline parallelism maximizes hardware utilization by eliminating the pipeline bubbles inherent in synchronous execution, offering a path toward efficient large-scale distributed training. However, this efficiency gain can be compromised by gradient staleness, where the immediate model updates with delayed gradients introduce noise into the optimization process. Crucially, we identify a critical, yet often overlooked, pathology: this delay scales linearly with pipeline depth, fundamentally undermining the very scalability that the method originally intends to provide. In this work, we investigate this inconsistency and bridge the gap by rectifying delayed gradients through basis rotation, restoring scalable asynchronous training while maintaining performance. Specifically, we observe that the deleterious effects of delayed gradients are exacerbated when the Hessian eigenbasis is misaligned with the standard coordinate basis. We demonstrate that this misalignment prevents coordinate-wise adaptive schemes, such as Adam, from effectively leveraging curvature-aware adaptivity. This failure leads to significant oscillations in the optimization trajectory and, consequently, slower convergence. We substantiate these findings through both rigorous theoretical analysis and empirical evaluation. To address this challenge, we propose the use of basis rotation, demonstrating that it effectively mitigates the alignment issue and significantly accelerates convergence in asynchronous settings. For example, our training of a 1B-parameter LLM with basis rotation achieves the same training loss in 76.8% fewer iterations compared to the best-performing asynchronous pipeline parallel training baseline.

^{*}Equal contribution ¹POSTECH. Correspondence to: Namhoon Lee <namhoon.lee@postech.ac.kr>.

1. Introduction

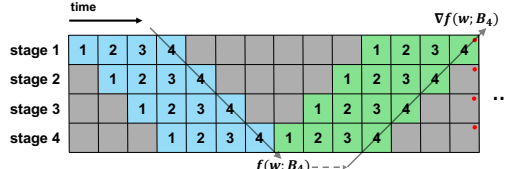
Training billion-parameter scale LLMs requires partitioning the model across multiple devices, as the memory footprint of such models far exceeds the capacity of individual accelerators. Pipeline parallelism addresses this by dividing the model into sequential stages, each allocated to a separate device. As a result, it has become a cornerstone of LLM training—alongside data, tensor, and context parallelism—as models continue to grow (Dubey et al., 2024; Adler et al., 2024; Liu et al., 2024; Yang et al., 2025; Team et al., 2025).

However, the efficiency of this approach is fundamentally constrained by its synchronous design, which mandates that each stage wait for the completion of backward passes of every other stage before updating its weights (Huang et al., 2019; Fan et al., 2021; Li & Hoefer, 2021). This dependency results in suboptimal hardware utilization by introducing significant idle periods, commonly referred to as pipeline bubbles.

Asynchronous pipeline parallelism aims to mitigate these idle periods by allowing each stage to proceed with subsequent computations without waiting for the completion of backward passes of other stages (Narayanan et al., 2019; 2021). While this approach significantly increases hardware utilization, it introduces gradient staleness as a consequence of the temporal gap between gradient calculation and application; *i.e.*, gradients arrive at the update step after the model has undergone multiple intervening weight updates (see Figure 1). This delayed arrival has emerged as a primary challenge in asynchronous training, as it often degrades convergence stability and final model performance (Yang et al., 2021; Ajanthan et al., 2025).

Notably, we find that gradient staleness presents a critical bottleneck, particularly for large models. This is because gradient delay increases alongside model size and pipeline depth; indeed, the number of stages can easily reach tens or hundreds in large-scale configurations¹. In fact, we observe that increasing the number of stages for a fixed model results in a drastic 5.81-fold slowdown in convergence speed in our experiments (see Figure 2a). This suggests that staleness is not merely a nuisance, but a fundamental barrier to the scalability of asynchronous pipelining, despite the fact that

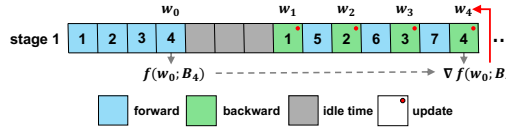
¹We provide an analysis of model-stage scaling in Appendix A.



(a) Synchronous pipeline parallelism



(b) Asynchronous pipeline parallelism



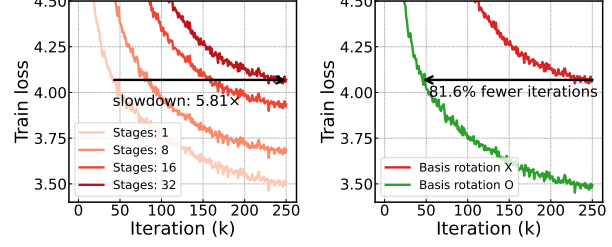
(c) Delay in asynchronous pipeline parallelism

Figure 1. (a-b) Schematic diagrams showing how micro-batches (blocks 1–7) are processed over time: a micro-batch travels from stage 1 to stage 4 in a forward pass (blue), and then goes back to stage 1 through a backward pass (green). Once the gradient becomes available after the backward pass, the model is updated (red dots indicate the time points). Asynchronous pipelining removes idle periods by processing subsequent micro-batches immediately after completing a backward pass without waiting for the completion of the pipeline cycle. (c) An illustration of model update with delayed gradient at stage 1: w_3 is updated to w_4 with $\nabla f(w_0; B_4)$.

asynchronous pipeline parallelism is designed to facilitate large-scale training.

Our analysis reveals that this degradation is deeply rooted in the interaction between delayed updates and the characteristics of Adam (Kingma & Ba, 2015), the de facto optimizer for LLM pre-training (Touvron et al., 2023b; Dubey et al., 2024; Liu et al., 2024). Specifically, we identify that Adam’s coordinate-wise adaptivity suffers significantly from delay under basis misalignment—a condition where the Hessian eigenbasis is not aligned with the standard coordinate basis. Intuitively, this misalignment induces large oscillations in the optimization trajectory, which amplifies the error introduced by delayed gradients. We substantiate this intuition through controlled empirical observations and a formal convergence analysis, establishing basis misalignment as a critical factor in the success of asynchronous optimization.

To address this, we propose mitigating the impact of staleness through basis rotation, a framework that transforms the optimization space to align the Hessian eigenbasis with the standard basis. We introduce several practical rotation strategies using different Hessian approximations and provide a theoretical analysis of their respective approxima-



(a) Impact of delay

(b) Effectiveness of solution

Figure 2. Summary of this work. (a) Impact of pipeline depth (i.e., number of stages) on convergence of asynchronous pipeline parallel LLM pre-training. In all cases, the model itself is kept the same while the number of stages is divided to be different. Increased delay leads to significant degradation on convergence speed. (b) Basis rotation substantially accelerates convergence in the presence of a large delay (here, for the case of 32 stages).

tion qualities. Empirical evaluations on LLM pre-training demonstrate that our proposed solution significantly neutralizes the degradation caused by gradient delay; for example, basis rotation helps to achieve the same training loss in up to 81.6% fewer iterations than the standard asynchronous pipeline parallel training (Figure 2b). These results suggest that basis rotation is a vital component for enabling high-fidelity, large-scale asynchronous pipeline parallelism.

Our key contributions are summarized as follows:

- Identifying a critical issue in scaled pipelines: We show that asynchronous pipeline parallel training suffers from significant convergence and model performance degradation as the number of stages increases, which has received limited formal study in the literature.
- Demystifying the mechanism of failure: We point out basis misalignment as the primary reason Adam-type optimizers are sensitive to delay. We provide both empirical evidence and theoretical convergence analysis to show how this misalignment exacerbates the negative impact of stale gradients (Section 2).
- The basis rotation framework: To mitigate these effects, we propose basis rotation, a method designed to realign the optimization trajectory and counteract the delay-induced instability under basis misalignment (Section 3).
- Empirical validation: We provide extensive experimental results, including evaluations on models at the 1B-parameter scale, demonstrating that our proposed solution effectively alleviates the performance penalties inherent in deep asynchronous pipelines (Section 4).

2. Understanding the Impact of Delay

While asynchronous pipeline parallelism offers significant throughput advantages, we find that the resulting gradient delay can lead to pathological training behaviors where increasing model scale can critically damage model performance. To resolve this issue, we suggest first understanding

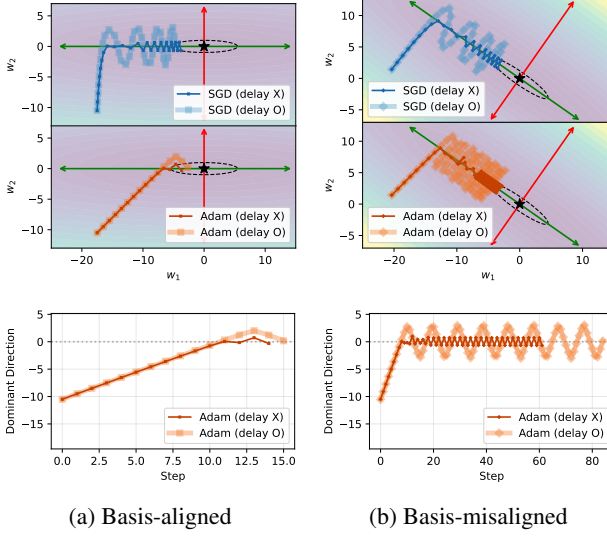


Figure 3. Impact of basis alignment on the effect of delay. (Top) Optimization trajectories of **SGD** and **Adam** with and without delay. (Bottom) Update of Adam along the dominant direction (red arrows in the top panel). (a) When the Hessian eigenbasis is aligned with the standard coordinate basis, Adam yields a stable trajectory and shows robustness to delay. (b) When two bases are misaligned, Adam exhibits strong oscillations along the dominant direction and suffers significantly from delay. See Appendix B.1 for experimental details.

the fundamental mechanisms of how delayed gradients interact with the optimization landscape. We attribute the degradation from delay primarily to misalignment between the Hessian eigenbasis and the standard coordinate basis, which we refer to as basis misalignment. Under such conditions, coordinate-wise adaptive optimizers such as Adam become vulnerable to delays.

2.1. Root of Degradation: Basis Misalignment

The heterogeneous curvature of Transformer loss landscapes renders a single global learning rate ineffective (Zhang et al., 2024; 2025b), establishing coordinate-wise adaptive optimizers like Adam as the de facto standard (Touvron et al., 2023b; Dubey et al., 2024). By adapting step sizes for each parameter individually, these optimizers effectively mitigate the oscillations that typically arise when the learning rate is excessive relative to local curvature (Kingma & Ba, 2015; Zhang et al., 2020; Pan & Li, 2023). We identify an implicit role of this adaptivity in asynchronous training: providing robustness against gradient delay. To illustrate this effect, we consider a quadratic optimization problem $\min_w \frac{1}{2} w^\top H w$ with a diagonal Hessian H (see Figure 3a). In this setting, SGD exhibits oscillatory updates along the dominant eigenvector direction (red arrows) while progressing slowly along non-dominant directions (green arrows). In contrast, Adam effectively suppresses these oscillations with adaptivity, yielding a stable and nearly direct trajectory toward the optimum. Crucially, this stability ensures that the

delayed update remains closely aligned with its non-delayed counterpart, rendering Adam robust to gradient staleness.

However, this robustness critically depends on the alignment between the Hessian eigenbasis and the coordinate system underlying the adaptive method. When this alignment is not secured, Adam fails to effectively exploit adaptivity and becomes vulnerable to the detrimental effects of delayed gradients. As shown in Figure 3b, under basis misalignment, Adam’s effective adaptivity diminishes and its trajectory resembles the behavior of SGD. In particular, severe oscillations occur along the dominant eigenvector direction, which we identify as the primary mechanism amplifying sensitivity to delay. When the trajectory oscillates rapidly, delayed gradients are likely to be stale—pointing in outdated or even adversarial directions relative to the current iterate—thereby substantially degrading convergence.

2.2. Empirical Observation

Building on the high-level intuition from quadratic optimization, we design a spiral loss landscape to better simulate the non-stationary geometry of deep neural networks where the Hessian eigenbasis evolves along the training trajectory. During training, we introduce synthetic delays at random points and quantify their impact using the slowdown ratio, defined as $T_{\text{delay}}/T_{\text{no-delay}}$, where T_{delay} and $T_{\text{no-delay}}$ each represent the number of iterations required to traverse a fixed angular interval with and without delay. See Appendix B.1 for the experimental details.

As shown in Figure 4a, Adam exhibits a stable trajectory with minimal oscillation when the Hessian eigenbasis aligns with the standard coordinate basis (see green boxes). In contrast, significant oscillation along the dominant direction emerges for the misaligned regions (see red boxes). Figure 4b directly correlates this instability with sensitivity to delay. We observe that the slowdown ratio is minimized near basis-aligned regions, indicating that delay has a negligible impact on convergence (see green dotted lines). In contrast, this ratio increases in misaligned regions where delay substantially impedes the convergence (see red dotted lines). These results support that basis misalignment renders coordinate-wise adaptive scheme of Adam-type optimizers susceptible to delay-induced convergence instability.

2.3. Theoretical Verification

Beyond the empirical observations, we provide a formal convergence analysis to demonstrate that Adam suffers significantly from delayed gradients under basis misalignment. Specifically, we prove that the negative effect of delay τ on the convergence rate is exacerbated for the basis-misaligned case compared to the aligned case. We first present assumptions necessary for our analysis.

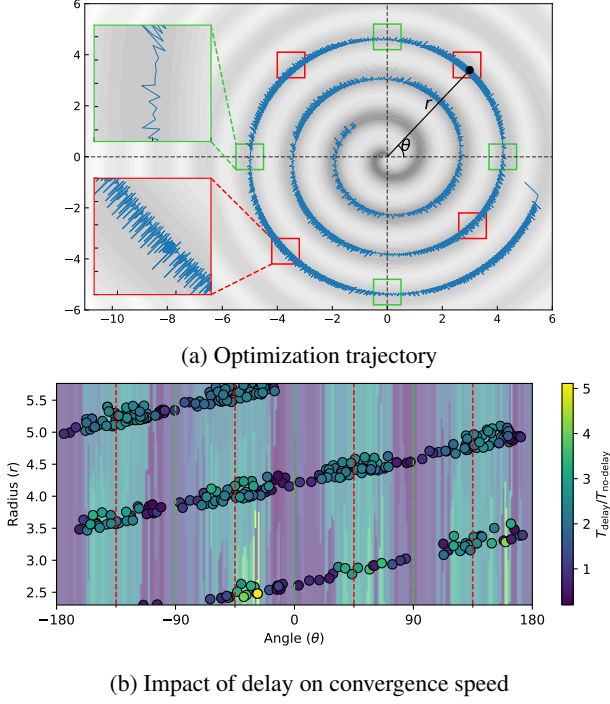


Figure 4. (a) Optimization trajectory of Adam on the spiral loss. The optimizer maintains a stable trajectory in basis-aligned regions (green boxes) but exhibits severe oscillations in misaligned regions (red boxes). (b) Slowdown ratio $T_{\text{delay}}/T_{\text{no-delay}}$ in different regions. The ratio is minimized near basis-aligned regions (green dotted lines), whereas it is maximized in misaligned regions (red dotted lines). This demonstrates that basis misalignment significantly amplifies the deleterious effects of delayed gradients.

Assumption 2.1. (Coordinate-wise bounded noise) For each coordinate $i \in \{1, \dots, d\}$, there exists σ_i such that $\mathbb{E}_\xi[\nabla_i f(w; \xi) - \mathbb{E}_\xi[\nabla_i f(w; \xi)]]^2 \leq \sigma_i^2$ for all $w \in \mathbb{R}^d$ where ξ denotes the stochasticity of data.

Assumption 2.2. (c -coordinate-wise ℓ_∞ smoothness) f is c -smooth coordinate-wisely w.r.t. ℓ_∞ norm with $c = (C_1, \dots, C_d) \in \mathbb{R}^d$, i.e., for each coordinate $i \in \{1, \dots, d\}$, $|\nabla_i f(w) - \nabla_i f(w')| \leq C_i \|w - w'\|_\infty$ for any $w, w' \in \mathbb{R}^d$. This implies that f is C -smooth w.r.t. ℓ_∞ norm where $C = \sum_{i=1}^d C_i$, i.e., $\|\nabla f(w) - \nabla f(w')\|_1 \leq C \|w - w'\|_\infty$ for all $w, w' \in \mathbb{R}^d$.

These coordinate-wise assumptions enable capturing Adam's coordinate-wise adaptivity in the convergence rate. Specifically, C locally corresponds to the $(1, 1)$ -norm of the Hessian matrix, defined as $\|\nabla^2 f(w)\|_{1,1} := \sum_{i,j} |(\nabla^2 f(w))_{i,j}|$. For a fixed eigenvalue spectrum, this norm is minimized when the Hessian is diagonal and increases under basis misalignment. Thus, it acts as a promising proxy for basis misalignment (Xie et al., 2025; Zhang et al., 2025a). We are now ready to present the convergence theorem for asynchronous Adam under delay.

Theorem 2.3. Let f be a non-convex function where Assumptions 2.1 and 2.2 hold. Define $\Delta_0 \triangleq (f(w_0) - \min_w f(w))$ as the initial suboptimality gap. Assume that initial second moment v_0 and step size η satisfy $v_0 + \epsilon > (\sum_{i=1}^d \sigma_i^2 + \|\nabla f(w_0)\|_\infty^2 + \sum_{i=1}^d C_i^2 \eta^2)/\text{poly}(T)$. Then, with appropriate choices of η and β_2 , the convergence rate of asynchronous Adam with $\beta_1 = 0$ under delay τ is as follows:

$$\begin{aligned} \min_{\frac{T}{2} < t \leq T} \mathbb{E} \|\nabla f(w_t)\|_1 \\ = \mathcal{O} \left(\sqrt{\frac{(1 + \tau)\Delta_0 C}{T}} + \sqrt{\sum_{i=1}^d \sigma_i^2 \left(\frac{(1 + \tau)\Delta_0 C}{T} \right)^{1/4}} \right. \\ \left. + \sum_{i=1}^d \sigma_i \left(\frac{\log T}{T} \right)^{1/4} \right). \end{aligned}$$

The proof is presented in Appendix C.

This result reveals that the impact of delay τ is tightly coupled with basis misalignment C as τ enters the bound multiplicatively with C . Specifically, for a fixed delay τ , the relative contribution of the delay-dependent terms to the total bound increases with C , thereby exacerbating the penalty for basis misalignment. Thus, while the effects of delay are suppressed for basis-aligned cases (i.e., small C), they are aggressively amplified for misaligned cases (i.e., large C) where the delay-dependent terms begin to dominate the bound. This formalizes our empirical observation that the impact of delay increases when the Hessian eigenbasis is misaligned with the standard basis.

Remark The result indicates that delay τ slows down the deterministic convergence rate from $\mathcal{O}(\sqrt{1/T})$ to $\mathcal{O}(\sqrt{(1 + \tau)/T})$, which aligns with the analysis from the asynchronous optimization literature (Stich & Karimireddy, 2020; Arjevani et al., 2020; Koloskova et al., 2022). Also, when $\tau = 0$, the result recovers the convergence rate of Adam under ℓ_∞ smoothness without delay (Xie et al., 2025).

3. Mitigating the Impact of Delay

Our previous analysis suggests that the negative effects of delay can be mitigated in a basis-aligned space. We propose to achieve this through basis rotation which transforms the optimization space to align the Hessian eigenbasis with the standard basis.

3.1. Basis Rotation

Standard Adam update

$$w_{t+1} = w_t - \eta_t \frac{\text{EMA}(\nabla f(w_t))}{\sqrt{\text{EMA}(\nabla f(w_t)^2) + \epsilon}} \quad (1)$$

Algorithm 1 Adam with Basis Rotation

```

1: for  $t = 1, 2, \dots, T$  do
2:   Sample batch  $B_t$ 
3:    $G_t \leftarrow \nabla f_W(W_t; B_t) \in \mathbb{R}^{m \times n}$ 
4:    $M_t \leftarrow \beta_1 M_{t-1} + (1 - \beta_1) G_t$ 
5:   if  $t \bmod \text{freq} = 0$  then
6:      $U, V \leftarrow \text{Eigenbasis-Estimation}$ 
7:   end if
8:    $\tilde{G}_t \leftarrow U^\top G_t V$ 
9:    $M_t \leftarrow U^\top M_t V$ 
10:   $\tilde{V}_t \leftarrow \beta_2 \tilde{V}_{t-1} + (1 - \beta_2) \tilde{G}_t \odot \tilde{G}_t$ 
11:   $W_{t+1} \leftarrow W_t - \eta_t U \left( \frac{1}{\sqrt{\tilde{V}_t + \epsilon}} \odot \tilde{M}_t \right) V^\top$ 
12: end for

```

relies on coordinate-wise scaling. As demonstrated in Section 2, this scaling becomes ineffective when the Hessian eigenbasis is misaligned with the standard basis, causing delayed gradients to introduce significant noise into the optimization process. The core idea of basis rotation is to mitigate the impact of delay by taking an optimization step in the basis-aligned coordinate system $\tilde{w} = \mathcal{U}^\top w$:

$$\tilde{w}_{t+1} = \tilde{w}_t - \eta_t \frac{\text{EMA}(\mathcal{U}^\top \nabla f(\mathcal{U}\tilde{w}_t))}{\sqrt{\text{EMA}((\mathcal{U}^\top \nabla f(\mathcal{U}\tilde{w}_t))^2)} + \epsilon}, \quad (2)$$

where \mathcal{U} is a rotation matrix whose columns are estimated eigenvectors of the Hessian. Projecting the update back onto the original space gives

$$w_{t+1} = w_t - \eta_t \mathcal{U} \frac{\text{EMA}(\mathcal{U}^\top \nabla f(w_t))}{\sqrt{\text{EMA}((\mathcal{U}^\top \nabla f(w_t))^2)} + \epsilon}. \quad (3)$$

Crucially, when \mathcal{U} perfectly aligns with the Hessian eigenbasis, the Hessian eigenbasis in the rotated space matches exactly with the standard coordinate basis. By ensuring that adaptive scaling is applied in the basis-aligned space, basis rotation restores the efficacy of curvature-aware adaptivity and mitigates the adverse effects of gradient delay.

The full procedure of basis rotation for a weight matrix $W \in \mathbb{R}^{m \times n}$ is detailed in Algorithm 1. To mitigate the prohibitive computational and memory costs for computing \mathcal{U} in Equation (3), basis rotation adopts two structural assumptions on the Hessian: (i) block-diagonality and (ii) Kronecker factorization. The former assumes a block-diagonal Hessian, enabling matrix-wise rotation rather than rotating the entire parameter space at once. This assumption is empirically supported in Transformer (Zhang et al., 2024; 2025b; Abreu et al., 2025). The latter allows the rotation matrix $\mathcal{U}_W \in \mathbb{R}^{mn \times mn}$ to be factorized into $U \in \mathbb{R}^{m \times m}$ and $V \in \mathbb{R}^{n \times n}$, making the rotation computationally tractable for large models (Martens & Grosse, 2015; Gupta et al., 2018; Vyas et al., 2025). Together with infrequent basis updates, basis rotation remains efficient at scale.

Algorithm 2 Eigenbasis-Estimation

```

Require: Approximation source  $\mathcal{S}$ , Rotation geometry  $\mathcal{G}$ 
1: if  $\mathcal{S} = 2^{\text{nd}}$  then
2:    $L \leftarrow \beta_2 L + (1 - \beta_2) G_t G_t^\top$ 
3:    $U \leftarrow \text{Power}(L, U)$ 
4:   if  $\mathcal{G} = \text{Bilateral}$  then
5:      $R \leftarrow \beta_2 R + (1 - \beta_2) G_t^\top G_t$ 
6:      $V \leftarrow \text{Power}(R, V)$ 
7:   end if
8:   if  $\mathcal{G} = \text{Unilateral}$  then
9:      $V \leftarrow I$ 
10:  end if
11: end if
12: if  $\mathcal{S} = 1^{\text{st}}$  then
13:    $U \leftarrow \text{Power}(M_t M_t^\top, U)$ 
14:   if  $\mathcal{G} = \text{Bilateral}$  then
15:      $V \leftarrow \text{Power}(M_t^\top M_t, V)$ 
16:   end if
17:   if  $\mathcal{G} = \text{Unilateral}$  then
18:      $V \leftarrow I$ 
19:   end if
20: end if

```

3.2. Eigenbasis Estimation

We now introduce efficient eigenbasis-estimation strategies which theoretically induce basis alignment under the assumptions of Section 3.1. These strategies are categorized along two design axes: approximation source (\mathcal{S}) and rotation geometry (\mathcal{G}). This taxonomy provides a unified design space for balancing estimation fidelity against memory efficiency, depending on the demands and constraints of the training environment.

The first axis \mathcal{S} determines the statistical source used to approximate the Hessian. The high-fidelity version (2^{nd}) utilizes the second moments $L = \mathbb{E}[GG^\top]$ and $R = \mathbb{E}[G^\top G]$ to approximate the empirical Fisher, where G is the gradient matrix. This quantity has frequently been used as a computationally efficient proxy for the Hessian (Roux et al., 2007; Singh & Alistarh, 2020; Frantar et al., 2021). In contrast, $\mathcal{S} = 1^{\text{st}}$ variant employs first-order moments ($\mathbb{E}[GG^\top] \approx \mathbb{E}[G]\mathbb{E}[G^\top]$), eliminating dedicated storage for L and R by leveraging the existing momentum buffer.

The second axis \mathcal{G} determines the rotation geometry used to diagonalize the approximating matrix. The bilateral version applies a two-sided rotation to capture the full Kronecker-factored structure, while the unilateral variant applies a one-sided rotation to the smaller dimension of the gradient. This reduces overhead by storing eigenvectors of either L or R , which is particularly beneficial for rectangular matrices.

These strategies can theoretically reduce the $(1, 1)$ -norm of the Hessian, which is a proxy for the degree of mis-

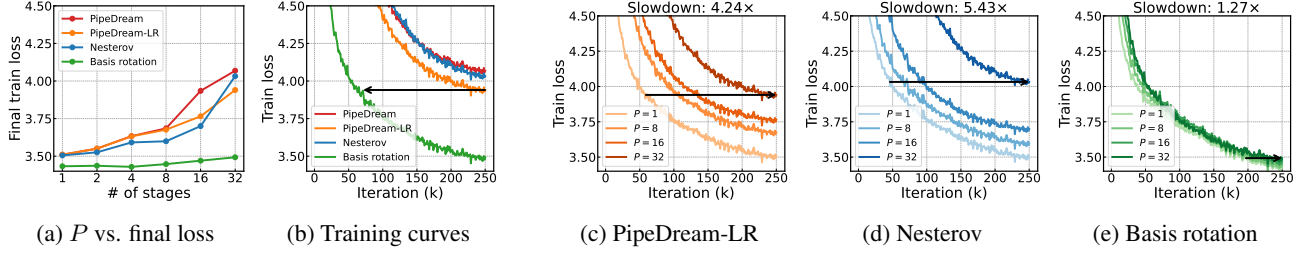


Figure 5. Performance of different methods when increasing the number of stages P for the same model (with 95M parameters). (a) Basis rotation maintains stable performance while baselines suffer significantly from delay. (b) Basis rotation shows much faster convergence under large delay compared to baselines (for $P = 32$). (c-e) Basis rotation reduces slowdown, *i.e.*, the iteration ratio required to reach target loss for $P = 32$ relative to $P = 1$, by a large margin compared to baselines. More results including other baselines are presented in Figures 11, 12, 15 and 16 of Appendix F.

alignment as introduced in Section 2.3. Define the rotated Hessians H_U and $H_{U,V}$ corresponding to the transformations $\tilde{W} = U^\top W$ (unilateral) and $\tilde{W} = U^\top WV$ (bilateral) respectively. Then, the following theorem holds.

Theorem 3.1. *Let U and V be the matrices whose columns are eigenvectors of $\mathbb{E}[GG^\top]$ and $\mathbb{E}[G^\top G]$ respectively. If Hessian admits a Kronecker-factorized empirical Fisher, the following inequalities hold:*

$$\|H_{U,V}\|_{(1,1)} \leq \|H_U\|_{(1,1)} \leq \|H\|_{(1,1)}.$$

Moreover, $\|H_{U,V}\|_{(1,1)}$ achieves the global minimum over all rotations.

The theorem shows that the bilateral rotation minimizes basis misalignment while both versions provide better alignment than the original space. The proof and further result for $\mathcal{S} = 1^{\text{st}}$ are provided in Appendix D.

The full procedure covering both axes is presented in Algorithm 2. We use a single step of power iteration followed by QR decomposition to efficiently compute eigenvectors (Wang et al., 2024). While our eigenbasis-estimation framework shares similarities with recent optimizers—such as SOAP (Vyas et al. (2025); $\mathcal{S} = 2^{\text{nd}}$, \mathcal{G} = bilateral) and the full-rank version of GaLore (Zhao et al. (2024); $\mathcal{S} = 1^{\text{st}}$, \mathcal{G} = unilateral)—we distinguish our approach by unifying these strategies into a single framework rather than adopting individual optimizers. This controlled setup allows us to isolate the effects of Hessian geometry from other implementation variables. See Appendix E for a detailed comparison.

4. Experiments

4.1. Experimental Setup

We evaluate the performance of basis rotation on the language modeling task with a standard decoder-only Transformer (Vaswani et al., 2017) ranging from 95M to 1B parameters. The models are trained on 1B tokens randomly

selected from OpenWebText (Gokaslan & Cohen, 2019). We evaluate basis rotation against three baselines which are primary strategies for asynchronous pipeline parallelism in the literature: (1) PipeDream (Narayanan et al., 2019) which serves as the vanilla baseline by not explicitly addressing delay, (2) PipeDream-LR (Yang et al., 2021) which schedules the stage-wise learning rate depending on the level of delay, and (3) Nesterov (Ajanthan et al., 2025) which incorporates Nesterov momentum to address delayed gradients. We use $\mathcal{S} = 2^{\text{nd}}$, \mathcal{G} = bilateral strategy for eigenbasis-estimation and set the basis update frequency to 10 unless specified otherwise. Finally, we employ weight stashing (Narayanan et al., 2019) across all methods to ensure consistency between the weights used in the forward and backward passes. Experimental details can be found in Appendix B.2.

4.2. Main Results

We first evaluate the robustness of basis rotation against delay by increasing the number of pipeline stages P for the same model. The results summarized in Figure 5a demonstrate that basis rotation consistently outperforms baselines with the performance gap widening significantly as P increases. While prior work has demonstrated the benefits of optimization in the Hessian eigenbasis under the standard zero-delay regime (Vyas et al., 2025; Eschenhagen et al., 2025), our results indicate that these advantages are substantially amplified in the presence of large delays. Notably, Figure 5b demonstrates that at $P = 32$, basis rotation achieves the same training loss with 71.6% fewer iterations than the best-performing baseline. To quantify robustness to delay, the right three panels of Figure 5 report the slowdown of each method, defined as the ratio of the number of iterations required to reach a fixed loss threshold at $P = 32$ relative to $P = 1$. As shown in Figures 5c and 5d, even the best-performing baseline shows a large slowdown of $4.24 \times$. In contrast, basis rotation in Figure 5e exhibits substantially improved robustness to delay with only $1.27 \times$ slowdown.

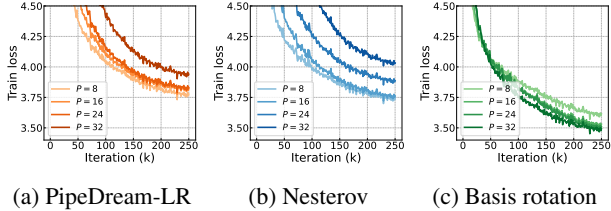


Figure 6. Performance of different methods when increasing P by scaling the number of blocks. While scaling the model leads to increased loss for baselines (a,b), it decreases the loss for basis rotation (c). More results are presented in Figure 13 of Appendix F.

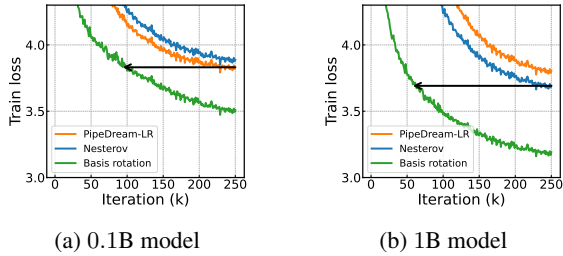


Figure 7. Performance of different methods at $P = 24$ for (a) 0.1B and (b) 1B models. The gap between basis rotation and baselines increases further for larger models.

Next, we investigate the scalability of basis rotation by jointly increasing the number of Transformer blocks and the number of pipeline stages P , assigning one block to each stage. This setup reflects the practical necessity of using deeper pipelines to accommodate the memory footprint of larger models. Figures 6a and 6b reveal a critical failure in baseline methods; increasing model size leads to higher training loss, directly contradicting standard scaling laws (Kaplan et al., 2020; Hoffmann et al., 2022). In contrast, basis rotation in Figure 6c successfully restores scalability, achieving consistent performance improvements as model size grows.

Finally, we evaluate basis rotation on a 1B parameter model to verify its efficacy at a larger scale. Specifically, we set $P = 24$ and increase the number of embedding dimensions to scale the model. Figure 7 demonstrates the performance gap between basis rotation and the baselines widens for larger models. For 1B model, basis rotation achieves the same training loss with 76.8% fewer iterations than the best-performing baseline, surpassing the 62.4% reduction in smaller models. The results show that the advantages of our approach scale positively with model size.

Overall, our results underscore that the performance degradation observed in asynchronous training is not an unavoidable cost of staleness but rather a byproduct of optimizer sensitivity to delay. Basis rotation effectively eliminates this bottleneck, unlocking a new regime for bubble-free execution at scale.

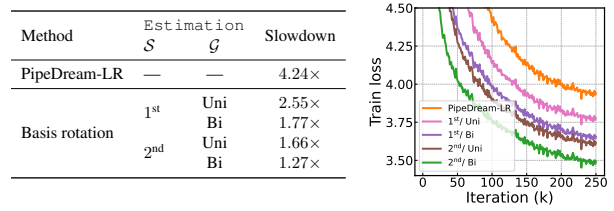


Figure 8. Comparison of different eigenbasis-estimation strategies. (a) High-fidelity estimation leads to a smaller slowdown under delay. (b) High-fidelity estimation achieves faster convergence for $P = 32$. Even the least accurate estimation (1st/unilateral) outperforms the best-performing baseline. More results are presented in Figure 14 of Appendix F.

4.3. More Results

Basis Approximation Sensitivity To evaluate how the precision of the eigenbasis approximation affects robustness to delay, we compare different eigenbasis-estimation strategies in Figure 8. As seen in Table 8a, basis rotation exhibits higher robustness with a closer approximation to the Hessian eigenbasis. Specifically, 2nd results in a smaller slowdown than 1st while bilateral outperforms unilateral. The results confirm that basis misalignment is the primary factor of the performance degradation under delay and a more accurate basis rotation effectively mitigates the issue. We also note that even the least accurate strategy (1st / unilateral) outperforms the best-performing baseline by a large margin (see Figure 8b). The results suggest that our approach is highly effective even in resource-constrained settings where more sophisticated estimation strategies may be computationally expensive.

Robustness without Weight Stashing The weight stashing employed throughout our main experiments ensures correct backpropagation by storing the weights used for the forward pass. However, it incurs memory overhead that scales linearly with the number of pipeline stages, making it prohibitive in memory-constrained environments. To evaluate whether the benefits of basis rotation persist in such resource-limited settings, we replace weight stashing with a PipeMare-style weight prediction which serves as a primary alternative to weight stashing (Yang et al., 2021). This technique reduces memory overhead by approximating the weights used for the forward pass albeit at the cost of incorrect gradient computation. Figure 9a shows that basis rotation remains effective in this scenario, maintaining a significant performance advantage over baselines. Notably, Figures 9b and 9c reveal that basis rotation remains robust without weight stashing whereas baselines exhibit severe degradation. This suggests that our approach is significantly more resilient to incorrect backpropagation.

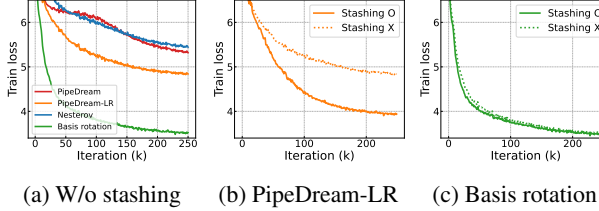


Figure 9. Performance of different methods when using PipeMare-style weight prediction (Yang et al., 2021) instead of weight stashing for $P = 32$. (a) Basis rotation outperforms baselines with a large margin. (b,c) While baselines exhibit severe degradation without weight stashing, basis rotation remains robust.

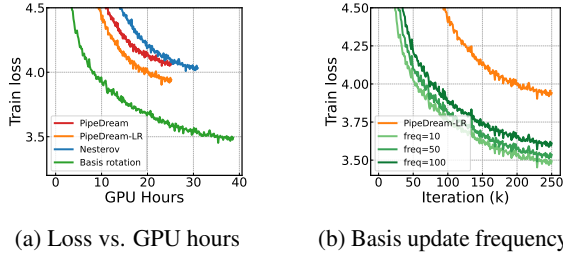


Figure 10. Efficiency of basis rotation. (a) Basis rotation outperforms other methods by a large margin in terms of GPU hours. (b) Basis rotation shows little performance degradation with infrequent basis updates.

Computational Efficiency To address potential concerns regarding the computational cost of the basis update, we compare its wall-clock efficiency against baselines. Figure 10a demonstrates that basis rotation remains superior in terms of GPU hours, reaching the same training loss with 54.3% less amount of time than the most competitive baselines. Furthermore, this overhead can be reduced by adjusting the basis update frequency with a marginal performance degradation. As shown in Figure 10b, basis rotation remains significantly more efficient than the baselines even at an update frequency of 100 iterations.

5. Related Works

Pipeline Parallelism GPipe (Huang et al., 2019) introduces synchronous pipeline parallelism but its efficiency is limited by pipeline bubbles. While several works propose advanced pipeline scheduling algorithms to improve device utilization, they still suffer from synchronization bottlenecks (Fan et al., 2021; Li & Hoefer, 2021). Asynchronous pipeline parallelism significantly maximizes throughput by entirely removing the synchronization step but exhibits performance degradation due to delayed gradients (Narayanan et al., 2019; 2021). Prior works address the issue with learning rate scheduling (Yang et al., 2021; Zhuang et al., 2021), Nesterov momentum (Ajanthan et al., 2025), and future weight prediction (Chen et al., 2018; Guan et al., 2019). However, these methods fail to effectively address delayed gradients under large-scale settings.

Adam for LLM Training Adam (Kingma & Ba, 2015) is widely used for training LLMs due to its superior performance over SGD. Recent works explain this success from various aspects including directional smoothness (Zhang et al., 2020; Pan & Li, 2023), heterogeneity of the Hessian spectrum in Transformers (Zhang et al., 2024), and heavy-tailed noise of language data (Kunstner et al., 2024). Meanwhile, Adam loses its advantage over SGD when the Hessian is not near-diagonal, or equivalently, when the Hessian eigenbasis is not aligned to the standard basis (Wang & Wiens, 2020; Zhang et al., 2025b). This is because Adam is not equivariant under rotation and its coordinate-wise adaptivity fails to work effectively for the basis-misaligned loss landscapes (Xie et al., 2025; Zhang et al., 2025a). We demonstrate that this problem exacerbates the impact of delay.

Hessian Approximation Hessian is often approximated via Gauss-Newton matrix (Schraudolph, 2002; Botev et al., 2017), Fisher (Amari, 1998; Martens, 2020), or empirical Fisher (Roux et al., 2007; Singh & Alistarh, 2020; Frantar et al., 2021), and their Kronecker-factored variants (Martens & Grosse, 2015; Gupta et al., 2018; Vyas et al., 2025). While Gauss-Newton and Fisher matrices serve as a robust proxy for the Hessian (Martens, 2020; Grosse, 2021), they require multiple backpropagation which leads to complex scheduling in asynchronous pipeline parallelism. Recent works show that Kronecker-factored empirical Fisher can serve as a practical surrogate for the Gauss-Newton matrix (Morwani et al., 2025). Based on these works, we utilize the eigenvectors of the Kronecker-factored empirical Fisher to perform basis rotation, ensuring a principled yet computationally tractable transformation.

6. Conclusion

In this work, we show that asynchronous pipeline parallelism is fundamentally challenged by gradient staleness: its convergence properties and model performance degrade critically as the delay grows with pipeline depth or model size. We identify that the root of this degradation lies in basis misalignment, which prevents a coordinate-wise adaptive optimizer from effectively navigating the loss landscape and leads to amplified oscillations under delay. To address this, we propose basis rotation, a framework that rotates the optimization space to realign the Hessian eigenbasis with the standard coordinate basis. Our extensive experiments show that basis rotation effectively neutralizes the impact of delay, significantly accelerating convergence in practical settings, and restoring scalable asynchronous training.

Acknowledgements

We thank Dongyeop Lee, Jinseok Chung, and Jihun Kim for helpful discussions during the early development of this project. This work was partly supported by the Institute of Information & communications Technology Planning & Evaluation (IITP) grant funded by the Korean government (MSIT) (RS-2019-II191906, Artificial Intelligence Graduate School Program (POSTECH) and the National Research Foundation of Korea (NRF) grant funded by the Korea government (MSIT) (RS-2023-00210466). Sungbin Shin was supported by Kwanjeong Educational Foundation Scholarship. Hyunji Jung was supported by the Korea Student Aid Foundation (KOSAF).

Impact Statement

This paper presents work aimed at advancing the field of machine learning by proposing basis rotation to mitigate delay in asynchronous pipeline parallelism. While the continued development of machine learning models has broad societal implications, there are no specific ethical concerns or negative consequences of this research that we feel must be highlighted here.

References

Abdin, M., Aneja, J., Behl, H., Bubeck, S., Eldan, R., Gunasekar, S., Harrison, M., Hewett, R. J., Javaheripi, M., Kauffmann, P., et al. Phi-4 technical report. *arXiv preprint arXiv:2412.08905*, 2024.

Abreu, N., Vyas, N., Kakade, S., and Morwani, D. The potential of second-order optimization for llms: A study with full gauss-newton. *arXiv preprint arXiv:2510.09378*, 2025.

Adler, B., Agarwal, N., Aithal, A., Anh, D. H., Bhattacharya, P., Brundyn, A., Casper, J., Catanzaro, B., Clay, S., Cohen, J., et al. Nemotron-4 340b technical report. *arXiv preprint arXiv:2406.11704*, 2024.

Ajanthan, T., Ramasinghe, S., Zuo, Y., Avraham, G., and Long, A. Nesterov method for asynchronous pipeline parallel optimization. *ICML*, 2025.

Amari, S.-I. Natural gradient works efficiently in learning. *Neural Computation*, 1998.

Arjevani, Y., Shamir, O., and Srebro, N. A tight convergence analysis for stochastic gradient descent with delayed updates. *ALT*, 2020.

Botev, A., Ritter, H., and Barber, D. Practical gauss-newton optimisation for deep learning. *ICML*, 2017.

Chen, C.-C., Yang, C.-L., and Cheng, H.-Y. Efficient and robust parallel dnn training through model parallelism on multi-gpu platform. *arXiv preprint arXiv:1809.02839*, 2018.

Dubey, A., Jauhri, A., Pandey, A., Kadian, A., Al-Dahle, A., Letman, A., Mathur, A., Schelten, A., Yang, A., Fan, A., et al. The llama 3 herd of models. *arXiv preprint arXiv:2407.21783*, 2024.

Eschenhagen, R., Defazio, A., Lee, T.-H., Turner, R. E., and Shi, H.-J. M. Purifying shampoo: Investigating shampoo’s heuristics by decomposing its preconditioner. *NeurIPS*, 2025.

Fan, S., Rong, Y., Meng, C., Cao, Z., Wang, S., Zheng, Z., Wu, C., Long, G., Yang, J., Xia, L., et al. Dapple: A pipelined data parallel approach for training large models. *PPOPP*, 2021.

Frantar, E., Kurtic, E., and Alistarh, D. M-fac: Efficient matrix-free approximations of second-order information. *NeurIPS*, 2021.

Gokaslan, A. and Cohen, V. Openwebtext corpus. <http://skylion007.github.io/OpenWebTextCorpus>, 2019.

Grosse, R. Adaptive gradient methods, normalization, and weight decay, 2021.

Guan, L., Yin, W., Li, D., and Lu, X. Xpipe: Efficient pipeline model parallelism for multi-gpu dnn training. *arXiv preprint arXiv:1911.04610*, 2019.

Gunter, T., Wang, Z., Wang, C., Pang, R., Narayanan, A., Zhang, A., Zhang, B., Chen, C., Chiu, C.-C., Qiu, D., et al. Apple intelligence foundation language models. *arXiv preprint arXiv:2407.21075*, 2024.

Gupta, V., Koren, T., and Singer, Y. Shampoo: Preconditioned stochastic tensor optimization. *ICML*, 2018.

Henderson, H. and Searle, S. The vec-permutation matrix, the vec operator and kronecker products: A review. *Linear & Multilinear Algebra*, 1981.

Hoffmann, J., Borgeaud, S., Mensch, A., Buchatskaya, E., Cai, T., Rutherford, E., Casas, D. d. L., Hendricks, L. A., Welbl, J., Clark, A., et al. Training compute-optimal large language models. *NeurIPS*, 2022.

Horn, R. A. and Johnson, C. R. *Topics in Matrix Analysis*. Cambridge University Press, 1991.

Huang, Y., Cheng, Y., Bapna, A., Firat, O., Chen, D., Chen, M., Lee, H., Ngiam, J., Le, Q. V., Wu, Y., et al. Gpipe: Efficient training of giant neural networks using pipeline parallelism. *NeurIPS*, 2019.

Jang, B., Yoo, I., and Yook, D. Pipelined stochastic gradient descent with taylor expansion. *Applied Sciences*, 2023.

Kaplan, J., McCandlish, S., Henighan, T., Brown, T. B., Chess, B., Child, R., Gray, S., Radford, A., Wu, J., and Amodei, D. Scaling laws for neural language models. *arXiv preprint arXiv:2001.08361*, 2020.

Karpathy, A. NanoGPT. <https://github.com/karpathy/nanoGPT>, 2022.

Kingma, D. P. and Ba, J. Adam: A method for stochastic optimization. *ICLR*, 2015.

Koloskova, A., Stich, S. U., and Jaggi, M. Sharper convergence guarantees for asynchronous sgd for distributed and federated learning. *NeurIPS*, 2022.

Korthikanti, V. A., Casper, J., Lym, S., McAfee, L., Anderesch, M., Shoeybi, M., and Catanzaro, B. Reducing activation recomputation in large transformer models. *MLSys*, 2023.

Kunstner, F., Milligan, A., Yadav, R., Schmidt, M., and Bietti, A. Heavy-tailed class imbalance and why adam outperforms gradient descent on language models. *NeurIPS*, 2024.

Li, S. and Hoefler, T. Chimera: efficiently training large-scale neural networks with bidirectional pipelines. *SC*, 2021.

Liu, A., Feng, B., Xue, B., Wang, B., Wu, B., Lu, C., Zhao, C., Deng, C., Zhang, C., Ruan, C., et al. Deepseek-v3 technical report. *arXiv preprint arXiv:2412.19437*, 2024.

Martens, J. New insights and perspectives on the natural gradient method. *JMLR*, 2020.

Martens, J. and Grosse, R. Optimizing neural networks with kronecker-factored approximate curvature. *ICML*, 2015.

Morwani, D., Shapira, I., Vyas, N., Malach, E., Kakade, S., and Janson, L. A new perspective on shampoo’s preconditioner. *ICLR*, 2025.

Narayanan, D., Harlap, A., Phanishayee, A., Seshadri, V., Devanur, N. R., Ganger, G. R., Gibbons, P. B., and Zaharia, M. Pipedream: Generalized pipeline parallelism for dnn training. *SOSP*, 2019.

Narayanan, D., Phanishayee, A., Shi, K., Chen, X., and Zaharia, M. Memory-efficient pipeline-parallel dnn training. *ICML*, 2021.

Pan, Y. and Li, Y. Toward understanding why adam converges faster than sgd for transformers. *arXiv preprint arXiv:2306.00204*, 2023.

Rajbhandari, S., Rasley, J., Ruwase, O., and He, Y. Zero: Memory optimizations toward training trillion parameter models. *SC*, 2020.

Robert, T., Safaryan, M., Modoranu, I.-V., and Alistarh, D. Ldadam: Adaptive optimization from low-dimensional gradient statistics. *ICLR*, 2025.

Roux, N., Manzagol, P.-A., and Bengio, Y. Topmoumoute online natural gradient algorithm. *NeurIPS*, 2007.

Schraudolph, N. N. Fast curvature matrix-vector products for second-order gradient descent. *Neural Computation*, 2002.

Shoeybi, M., Patwary, M., Puri, R., LeGresley, P., Casper, J., and Catanzaro, B. Megatron-lm: Training multi-billion parameter language models using model parallelism. *arXiv preprint arXiv:1909.08053*, 2019.

Singh, S. P. and Alistarh, D. Woodfisher: Efficient second-order approximation for neural network compression. *NeurIPS*, 2020.

Stich, S. U. and Karimireddy, S. P. The error-feedback framework: Better rates for sgd with delayed gradients and compressed communication. *JMLR*, 2020.

Team, K., Bai, Y., Bao, Y., Chen, G., Chen, J., Chen, N., Chen, R., Chen, Y., Chen, Y., Chen, Y., et al. Kimi k2: Open agentic intelligence. *arXiv preprint arXiv:2507.20534*, 2025.

Team, Q. et al. Qwen2 technical report. *arXiv preprint arXiv:2407.10671*, 2(3), 2024.

Touvron, H., Lavril, T., Izacard, G., Martinet, X., Lachaux, M.-A., Lacroix, T., Rozière, B., Goyal, N., Hambro, E., Azhar, F., et al. Llama: Open and efficient foundation language models. *arXiv preprint arXiv:2302.13971*, 2023a.

Touvron, H., Martin, L., Stone, K., Albert, P., Almahairi, A., Babaei, Y., Bashlykov, N., Batra, S., Bhargava, P., Bhosale, S., et al. Llama 2: Open foundation and fine-tuned chat models. *arXiv preprint arXiv:2307.09288*, 2023b.

Vaswani, A., Shazeer, N., Parmar, N., Uszkoreit, J., Jones, L., Gomez, A. N., Kaiser, Ł., and Polosukhin, I. Attention is all you need. *NeurIPS*, 2017.

Vyas, N., Morwani, D., Zhao, R., Kwun, M., Shapira, I., Brandfonbrener, D., Janson, L., and Kakade, S. Soap: Improving and stabilizing shampoo using adam. *ICLR*, 2025.

Wang, J. and Wiens, J. Adasgd: Bridging the gap between sgd and adam. *arXiv preprint arXiv:2006.16541*, 2020.

Wang, S., Zhou, P., Li, J., and Huang, H. 4-bit shampoo for memory-efficient network training. *NeurIPS*, 2024.

Xie, S., Mohamadi, M. A., and Li, Z. Adam exploits ℓ_∞ -geometry of loss landscape via coordinate-wise adaptivity. *ICLR*, 2025.

Yang, A., Yu, B., Li, C., Liu, D., Huang, F., Huang, H., Jiang, J., Tu, J., Zhang, J., Zhou, J., et al. Qwen2. 5-1m technical report. *arXiv preprint arXiv:2501.15383*, 2025.

Yang, B., Zhang, J., Li, J., Ré, C., Aberger, C., and De Sa, C. Pipemare: Asynchronous pipeline parallel dnn training. *MLSys*, 2021.

Zhang, J., He, T., Sra, S., and Jadbabaie, A. Why gradient clipping accelerates training: A theoretical justification for adaptivity. *ICLR*, 2020.

Zhang, T. H., Maes, L., Milligan, A., Jolicoeur-Martineau, A., Mitliagkas, I., Scieur, D., Lacoste-Julien, S., and Guille-Escuret, C. Understanding adam requires better rotation dependent assumptions. *NeurIPS*, 2025a.

Zhang, Y., Chen, C., Ding, T., Li, Z., Sun, R., and Luo, Z. Why transformers need adam: A hessian perspective. *NeurIPS*, 2024.

Zhang, Y., Chen, C., Li, Z., Ding, T., Wu, C., Kingma, D. P., Ye, Y., Luo, Z.-Q., and Sun, R. Adam-mini: Use fewer learning rates to gain more. *ICLR*, 2025b.

Zhao, J., Zhang, Z., Chen, B., Wang, Z., Anandkumar, A., and Tian, Y. Galore: Memory-efficient llm training by gradient low-rank projection. *ICML*, 2024.

Zheng, S., Meng, Q., Wang, T., Chen, W., Yu, N., Ma, Z.-M., and Liu, T.-Y. Asynchronous stochastic gradient descent with delay compensation. *ICML*, 2017.

Zhuang, H., Wang, Y., Liu, Q., and Lin, Z. Fully decoupled neural network learning using delayed gradients. *TNNLS*, 2021.

Contents

1	Introduction	1
2	Understanding the Impact of Delay	2
2.1	Root of Degradation: Basis Misalignment	3
2.2	Empirical Observation	3
2.3	Theoretical Verification	3
3	Mitigating the Impact of Delay	4
3.1	Basis Rotation	4
3.2	Eigenbasis Estimation	5
4	Experiments	6
4.1	Experimental Setup	6
4.2	Main Results	6
4.3	More Results	7
5	Related Works	8
6	Conclusion	8
A	Analysis for the Number of Stages for Pipeline Parallelism	13
B	Experimental Details	14
B.1	Section 2	14
B.2	Section 4	14
C	Proof of Theorem 2.3	15
D	Proof of Basis Misalignment Analysis	20
D.1	Proof of Theorem 3.1	20
D.2	Basis misalignment Analysis for $S = 1^{\text{st}}$	21
E	Connection to Recent Optimizers	22
F	More Experimental Results	22

A. Analysis for the Number of Stages for Pipeline Parallelism

This analysis analyzes the number of stages for pipeline parallelism when training LLMs of varying sizes. We calculate the minimum number of pipeline stages required to fit different model architectures onto standard GPU devices with different memory capacities. By modeling the memory footprint of a single Transformer block including parameters, optimizer states, and activation, we derive a formula to determine how many blocks can fit on a single device, and consequently, how many devices (stages) are needed for the full model.

Setting We assume a standard training recipe commonly used for dense LLMs. Specifically, we assume mixed precision training with AdamW optimizer for a standard Transformer architecture. We assume that gradient checkpointing is applied at the beginning of each Transformer block while weight stashes are offloaded to CPU to save memory. We only employ pipeline parallelism and do not use context, tensor, or fully sharded data parallelism. This is because these strategies require frequent collective communications and can be impractical for low-bandwidth settings (Rajbhandari et al., 2020; Shoeybi et al., 2019).

Notation We denote the embedding dimension, the number of attention heads, and the sequence length as h , a , and s respectively. We also denote batch size as b . W represents the number of parameters in a single Transformer block. L represents the total number of Transformer blocks.

Memory required for a single block To determine the number of stages, we first calculate the memory required for a single Transformer block. The memory consumption for one Transformer block consists of parameters, gradients, optimizer states, and activations. Assuming mixed-precision training, we need the following memory: (1) $2W$ bytes for half-precision parameters, (2) $2W$ bytes for half-precision gradients, (3) $4W + 4W + 4W = 12W$ bytes for full-precision optimizer states (each corresponding to full-precision master weights, first momentum, and second momentum), (4) $\approx 34sbh + 5bas^2$ bytes for activations. The memory for activation is the result from Korthikanti et al. (2023). Summing these components, the total memory required for a single block, M_{block} , is

$$M_{\text{block}} = 16W + 34sbh + 5bas^2 \quad (\text{bytes}) \quad (4)$$

Consequently, the total memory for N blocks is $N \times M_{\text{block}}$.

Calculating Required Stages Let m be the memory capacity of a single device (in bytes). We calculate N_{\max} , the maximum number of Transformer blocks that can fit on a single device, using the inequality:

$$NM_{\text{block}} \leq m, \quad (5)$$

which leads to $N_{\max} = \left\lfloor \frac{m}{16W + 34sbh + 5bas^2} \right\rfloor$. Based on N_{\max} , the minimum number of pipeline stages P required to host the full model (which has L total blocks) is determined as follows: (1) when $N_{\max} \geq 1$, at least one block fits on a device and $P = \left\lceil \frac{L}{N_{\max}} \right\rceil$ ², and (2) when $N_{\max} = 0$, a single device cannot hold even one Transformer block and $P \geq 2L$ (since we require at least two stages to allocate a single block).

We calculate the required number of stages (P) for various LLaMA models (Touvron et al., 2023a; Dubey et al., 2024) across different GPU hardware. Specifically, we assume a batch size of 1 for simplicity, *i.e.*, $b = 1$. We also assume a sequence length of 4096, *i.e.*, $s = 4096$, which are typically used for initial-phase training of recent LLMs (Touvron et al., 2023b; Team et al., 2024; Gunter et al., 2024; Abdin et al., 2024). We note that recent LLMs typically use much larger values of b and s so the number of required stages may increase further.

²This is when we ignore the memory needed for loading embedding layers and language model head. The number of stages may further increase for large embedding layers.

Table 9. Number of required stages (P) for different LLaMA models with sequence length $s = 4096$ and batch size $b = 1$. Values marked with * indicate that a single Transformer block cannot fit on one device ($N_{max} = 0$).

Model	h	a	W	L	RTX3070 (8GB)	RTX3080 (16GB)	RTX3090 (24GB)	A6000 (48GB)	A100 (80GB)
Llama 3.2 1B	2048	32	$\approx 67M$	16	16	6	4	2	1
Llama 3.2 3B	3072	24	$\approx 113M$	28	28	10	6	3	2
LLaMA 1-7B	4096	32	$\approx 202M$	32	32	16	11	5	3
LLaMA 1-13B	5120	40	$\approx 317M$	40	$\geq 80^*$	40	20	8	5
LLaMA 1-33B	6656	52	$\approx 535M$	60	$\geq 120^*$	60	60	20	12
LLaMA 1-65B	8192	64	$\approx 810M$	80	$\geq 160^*$	$\geq 160^*$	80	40	20
Llama 3.1 405B	16384	128	$\approx 3.19B$	126	$\geq 512^*$	$\geq 512^*$	$\geq 512^*$	$\geq 512^*$	126

The results are presented in Table 9. For devices with small memory (e.g., RTX3070), we need at least 80 stages even for 13B models. For larger models, the number of stages easily increases to hundreds. Even with a device with larger memory (e.g., A6000), we need tens of stages for moderate-size models (e.g., 33B, 65B). This analysis confirms that the number of stages in pipeline parallelism can easily reach tens or hundreds for the case of LLMs.

B. Experimental Details

B.1. Section 2

Section 2.1: Figure 3 To compare Adam’s coordinate-wise adaptivity with SGD, we employed AdaSGD (Wang & Wiens, 2020), which scales a uniform learning rate across all parameters by taking the exponential moving average of the average second momentum. This setup enabled us to use an identical learning rate for both AdaSGD and Adam, facilitating a direct comparison of how gradient delay interacts with coordinate-wise adaptivity. We set the learning rate to 1.0 and $\beta_1 = 0$ in order to isolate the adversarial update directions induced by delayed gradients without the confounding effect of momentum. For β_2 , we used 0.1 which is smaller than the standard Adam setting, to more clearly visualize oscillatory behavior. Nevertheless, our empirical analysis in Section 2.2 confirms that this alignment-dependent instability persists even with standard hyperparameters in practical training scenarios. Finally, we defined the convergence criterion as reaching a loss of 15.0 for each optimizer, tested with and without a delay of $\tau = 2$.

Section 2.2: Figure 4 The spiral loss landscape was defined as $f(r, \theta) = r^2 + (20 \sin(4r - \theta) + 1)^2$, where r and θ represent the radius and angle in polar coordinates. We set the learning rate to 0.1 and $\beta_1 = 0$ to focus on the effect of delayed gradients without momentum. We used $\beta_2 = 0.9$, matching standard Adam settings. Even with such a large β_2 , Adam exhibited low oscillation when the Hessian eigenbasis is aligned with the standard coordinate basis, whereas severe oscillations emerge in the misaligned case. For Figure 4b, we introduced a delay of $\tau = 1$ at a randomly chosen iteration during training without delay. We then measured the number of iterations required to traverse an angular displacement of 3° with and without delay, and report their ratio as the slowdown metric.

B.2. Section 4

Our model is based on nanoGPT (Karpathy, 2022). The model has an embedding dimension of 384, sequence length of 512, 6 attention heads, and 32 Transformer blocks. The model has learnable positional embedding and untied language model head. When the number of stages is P , we allocate $32/P$ Transformer blocks to each stage. The first and the last stage also hold embedding and language model head respectively. This model has approximately 96 million parameters.

The model is trained in bf16 mixed precision. We use the batch size of 8, which is the maximum without incurring out-of-memory error in our setting, and do not use gradient accumulation since it changes the level of delay (Ajanthan et al., 2025). For each method and stage, we search the learning rate among $\{0.0001, 0.0003, 0.001\}$. β_1 is set to 0.99 for Nesterov following the original paper (Ajanthan et al., 2025) and set to 0.9 for others. We use β_2 of 0.999, gradient clipping value of 1.0, and weight decay of 0.01. Unless specified otherwise, we set the basis update frequency to 10 for basis rotation. We only perform rotation to the MLP and attention layers excluding embedding layers, language model head, bias parameters, and layer normalization parameters. We use at most eight RTX 3090 GPUs for the experiments.

Our 1B model has an embedding dimension of 1728, sequence length of 512, 27 attention heads, and 24 Transformer blocks. The model has approximately 1.03 billion parameters. We use the learning rate of 0.0001. We use at most six A100 GPUs for these experiments.

C. Proof of Theorem 2.3

In this section, we present the proof of Theorem 2.3. In the following, we use H_i instead of C_i defined in Assumption 2.2.

We first present several lemmas necessary for the proof. The lemmas are taken from Xie et al. (2025) for the case of Adam.

Lemma C.1. (Corollary of Lemma 3.13. of Xie et al. (2025)) For any twice differentiable loss which is H -coordinate-wisely-smooth w.r.t. ℓ_∞ norm, we have for any x and $\Delta \in \mathbb{R}^d$,

$$|\Delta^\top \nabla^2 f(x) \Delta| \leq \sum_{i=1}^d H_i \Delta_i^2.$$

Lemma C.2. (Lemma 3.14. of Xie et al. (2025)) For any $0 < \beta_2 < 1$, for any scalar sequences $\{v_t\}_{t=0}^T$ and $\{g_t\}_{t=1}^T$ satisfying $v_0 \geq 0$, $v_1 > 0$, and $v_t - \beta_2 v_{t-1} \geq (1 - \beta_2) g_t^2$ for $t \geq 1$, the following holds:

$$\sum_{t=1}^T \frac{g_t^2}{v_t} \leq T + \frac{\beta_2}{1 - \beta_2} \ln \frac{v_T}{v_0}.$$

Lemma C.3. (Corollary of Lemma 3.15. of Xie et al. (2025)) Under the H -coordinate-wisely smoothness assumption, for any $i \in [d]$, the following holds:

$$\mathbb{E} \sum_{t=1}^T \frac{g_{t,i} \bar{g}_{t,i}}{\sqrt{v_{t,i} + \epsilon}} \geq \frac{1}{2} \mathbb{E} \sum_{t=1}^T \frac{\bar{g}_{t,i}^2}{\sqrt{\tilde{v}_{t,i} + \epsilon}} - \sqrt{1 - \beta_2} T \sigma_i - \frac{\sigma_i \beta_2}{\sqrt{1 - \beta_2}} \mathbb{E} \left[\ln \frac{v_{T,i} + \epsilon}{v_{0,i} + \epsilon} \right],$$

where \tilde{v} is defined as $\tilde{v}_{t,i} = (1 - \beta_2)(\bar{g}_{t,i}^2 + \sigma_i^2) + \beta_2 v_{t-1,i}$ and g_t and \bar{g}_t are stochastic the full-batch gradient respectively.

Lemma C.4. (Corollary of Lemma 3.16. of Xie et al. (2025)) With Assumption 2.2, for any $i \in [d]$, the following holds:

$$\sum_{t=\frac{T}{2}+1}^T \mathbb{E} \left[\sqrt{\tilde{v}_{t,i} + \epsilon} \right] \leq \frac{2\beta_2^{\frac{T}{2}}}{1 - \beta_2} \sqrt{v_{0,i}} + \frac{T}{2} \sigma_i + \frac{T}{2} \sqrt{\epsilon} + 2 \sum_{t=1}^T \mathbb{E} \left[\frac{\bar{g}_{t,i}^2}{\sqrt{\tilde{v}_{t,i} + \epsilon}} \right]$$

Lemma C.5. (Corollary of Lemma C.1. of Xie et al. (2025)) For any T , the following holds:

$$\ln \frac{\mathbb{E} \max_{i \in [d]} v_{T,i} + \epsilon}{v_0 + \epsilon} \leq 2 \ln \left(1 + \frac{\sum_{i=1}^d \sigma_i^2 + \|\nabla f(x_0)\|_\infty^2 + \sum_{i=1}^d H_i^2 \eta^2 T (T + \frac{1}{1 - \beta_2})}{v_0 + \epsilon} + \ln 32 \right)$$

Now, we are ready to prove Theorem 2.3. The key step for analyzing the convergence rate is to address the (B) term in Equation (1).

Proof. First, by the Taylor approximation, we have

$$f(x_{t+1}) = f(x_t) + \nabla f(x_t)(x_{t+1} - x_t) + \frac{1}{2} (x_{t+1} - x_t)^\top \nabla^2 f(x) (x_{t+1} - x_t)$$

for some x .

By Lemma C.1,

$$\begin{aligned}
 f(x_{t+1}) - f(x_t) &= \nabla f(x_t)(x_{t+1} - x_t) + \frac{1}{2}(x_{t+1} - x_t)^\top \nabla^2 f(x)(x_{t+1} - x_t) \\
 &\leq \nabla f(x_t)(x_{t+1} - x_t) + \frac{1}{2} \sum_{i=1}^d H_i (x_{t+1,i} - x_{t,i})^2 \\
 &= -\eta \sum_{i=1}^d \frac{g_{t-\tau,i} \bar{g}_{t,i}}{\sqrt{v_{t-\tau,i} + \epsilon}} + \frac{1}{2} \eta^2 \sum_{i=1}^d H_i \frac{g_{t-\tau,i}^2}{v_{t-\tau,i} + \epsilon} \\
 &= \underbrace{-\eta \sum_{i=1}^d \frac{\bar{g}_{t-\tau,i} g_{t-\tau,i}}{\sqrt{v_{t-\tau,i} + \epsilon}}}_{(A)} + \underbrace{\eta \sum_{i=1}^d \frac{(\bar{g}_{t-\tau,i} - \bar{g}_{t,i}) g_{t-\tau,i}}{\sqrt{v_{t-\tau,i} + \epsilon}}}_{(B)} + \underbrace{\frac{1}{2} \eta^2 \sum_{i=1}^d H_i \frac{g_{t-\tau,i}^2}{v_{t-\tau,i} + \epsilon}}_{(C)}. \tag{1}
 \end{aligned}$$

Note that we have added and subtracted $-\eta \sum_{i=1}^d \frac{\bar{g}_{t-\tau,i} g_{t-\tau,i}}{\sqrt{v_{t-\tau,i} + \epsilon}}$ so that we can use Lemma C.3. Since (A) and (C) can be upper bounded with Lemma C.3 and Lemma C.2 respectively, the remaining step is to upper bound (B).

By Cauchy-Schwarz inequality, we have

$$\eta \sum_{i=1}^d \frac{(\bar{g}_{t-\tau,i} - \bar{g}_{t,i}) g_{t-\tau,i}}{\sqrt{v_{t-\tau,i} + \epsilon}} \leq \eta \underbrace{\sqrt{\sum_{i=1}^d (\bar{g}_{t-\tau,i} - \bar{g}_{t,i})^2}}_{A_t} \cdot \underbrace{\sqrt{\sum_{i=1}^d \frac{g_{t-\tau,i}^2}{v_{t-\tau,i} + \epsilon}}}_{B_t}.$$

Summing over t and applying Cauchy-Schwarz inequality leads to

$$\eta \sum_{t=1}^{T+\tau} A_t B_t \leq \eta \sqrt{\sum_{t=1}^{T+\tau} A_t^2} \sqrt{\sum_{t=1}^{T+\tau} B_t^2}.$$

We can upper bound $\sqrt{\sum_{t=1}^T A_t^2}$ as follows.

$$\begin{aligned}
 \sqrt{\sum_{t=1}^{T+\tau} A_t^2} &= \sqrt{\sum_{t=1}^{T+\tau} \sum_{i=1}^d (\bar{g}_{t,i} - \bar{g}_{t-\tau,i})^2} \\
 &\leq \sqrt{\sum_{t=1}^{T+\tau} \sum_{i=1}^d H_i^2 \|x_t - x_{t-\tau}\|_\infty^2} \\
 &\leq \sqrt{\sum_{t=1}^{T+\tau} \sum_{i=1}^d H_i^2 \|x_t - x_{t-\tau}\|_2^2} \\
 &= \sqrt{\sum_{t=1}^{T+\tau} \sum_{i=1}^d H_i^2 \left\| \sum_{k=1}^{\tau} \eta \frac{g_{t-k-\tau}}{\sqrt{v_{t-k-\tau} + \epsilon}} \right\|_2^2} \\
 &\leq \sqrt{\sum_{t=1}^{T+\tau} \sum_{i=1}^d H_i^2 \tau \eta^2 \sum_{k=1}^{\tau} \left\| \frac{g_{t-k-\tau}}{\sqrt{v_{t-k-\tau} + \epsilon}} \right\|_2^2} \\
 &= \sqrt{\tau \eta^2 \sum_{t=1}^{T+\tau} \sum_{i=1}^d H_i^2 \sum_{k=1}^{\tau} \left\| \frac{g_{t-k-\tau}}{\sqrt{v_{t-k-\tau} + \epsilon}} \right\|_2^2} \\
 &= \sqrt{\tau \eta^2 \sum_{i=1}^d H_i^2 \sum_{t=1}^{T+\tau} \sum_{k=1}^{\tau} \left\| \frac{g_{t-k-\tau}}{\sqrt{v_{t-k-\tau} + \epsilon}} \right\|_2^2} \\
 &\leq \sqrt{\tau \eta^2 \sum_{i=1}^d H_i^2 \tau \sum_{t=1}^{T+\tau} \left\| \frac{g_{t-\tau}}{\sqrt{v_{t-\tau} + \epsilon}} \right\|_2^2} \\
 &= \tau \eta \sqrt{\sum_{i=1}^d H_i^2} \cdot \sqrt{\sum_{t=1}^{T+\tau} \left\| \frac{g_{t-\tau}}{\sqrt{v_{t-\tau} + \epsilon}} \right\|_2^2} \\
 &= \tau \eta \sqrt{\sum_{i=1}^d H_i^2} \cdot \sqrt{\sum_{t=1}^T \sum_{i=1}^d \frac{g_{t,i}^2}{v_{t,i} + \epsilon}}
 \end{aligned}$$

We have used Assumption 2.2 for the first inequality. The second inequality holds because ℓ_∞ norm of a vector is always smaller than or equal to its ℓ_2 norm. We have used Jensen's inequality for the third inequality. The final inequality holds because each term $\frac{g_{t-\tau}}{\sqrt{v_{t-\tau} + \epsilon}}$ is summed at most τ times.

Thus, we have

$$\begin{aligned}
 \eta \sum_{t=1}^T A_t B_t &\leq \eta \sqrt{\sum_{t=1}^T A_t^2} \sqrt{\sum_{t=1}^T B_t^2} \\
 &\leq \tau \eta^2 \sqrt{\sum_{i=1}^d H_i^2} \cdot \sum_{t=1}^T \sum_{i=1}^d \frac{g_{t-\tau,i}^2}{v_{t-\tau,i} + \epsilon}.
 \end{aligned} \tag{2}$$

Next, applying Lemma C.3 to (A) of Equation (1) gives

$$\begin{aligned}
 \sum_{t=1}^{T+\tau} \mathbb{E}(A) &= -\eta \sum_{t=1}^{T+\tau} \sum_{i=1}^d \mathbb{E} \frac{\bar{g}_{t-\tau,i} g_{t-\tau,i}}{\sqrt{v_{t-\tau,i} + \epsilon}} \\
 &= -\eta \sum_{i=1}^d \sum_{t=1}^T \mathbb{E} \frac{\bar{g}_{t,i} g_{t,i}}{\sqrt{v_{t,i} + \epsilon}} \\
 &\leq -\eta \sum_{i=1}^d \frac{1}{2} \mathbb{E} \sum_{t=1}^T \frac{\bar{g}_{t,i}^2}{\sqrt{\tilde{v}_{t,i}^2 + \epsilon}} + \eta \sum_{i=1}^d \sqrt{1 - \beta_2} T \sigma_i + \eta \sum_{i=1}^d \frac{\sigma_i \beta_2}{\sqrt{1 - \beta_2}} \mathbb{E} \left[\ln \frac{v_{T,i} + \epsilon}{v_{0,i} + \epsilon} \right].
 \end{aligned}$$

Then, by summing over t from $t = 0$ to T_τ , dividing by T , applying Lemma C.2 to (C) and Equation (2), and rearranging the terms, we get the following.

$$\begin{aligned}
 \frac{1}{T} \mathbb{E} \left[\sum_{i=1}^d \sum_{t=1}^{T+\tau} \frac{\bar{g}_{t-\tau,i}^2}{\sqrt{\tilde{v}_{t-\tau,i} + \epsilon}} \right] &= \frac{1}{T} \mathbb{E} \left[\sum_{i=1}^d \sum_{t=1}^T \frac{\bar{g}_{t,i}^2}{\sqrt{\tilde{v}_{t,i} + \epsilon}} \right] \\
 &\leq \frac{2}{\eta T} \mathbb{E}[f(x_0) - f(x_{T+\tau})] + \frac{\eta}{T} \mathbb{E} \left[\sum_{i=1}^d H_i \left(T + \frac{\beta_2}{1 - \beta_2} \ln \frac{v_{T,i} + \epsilon}{v_{0,i} + \epsilon} \right) \right] \\
 &\quad + \frac{2}{T} \sum_{i=1}^d \sigma_i \sqrt{1 - \beta_2} \left(T + \frac{\beta_2}{1 - \beta_2} \mathbb{E} \ln \frac{v_{T,i} + \epsilon}{v_{0,i} + \epsilon} \right) \\
 &\quad + \frac{2}{T} \tau \eta \sqrt{\sum_{i=1}^d H_i^2} \mathbb{E} \sum_{i=1}^d \left(T + \frac{\beta_2}{1 - \beta_2} \ln \frac{v_{T,i} + \epsilon}{v_{0,i} + \epsilon} \right) \\
 &\leq \frac{2}{\eta T} \mathbb{E}[f(x_0) - \min_x f(x)] + \eta \sum_{i=1}^d H_i + 2\sqrt{1 - \beta_2} \sum_{i=1}^d \sigma_i + 2\tau \eta \sqrt{\sum_{i=1}^d H_i^2} \\
 &\quad + \frac{\beta_2}{T(1 - \beta_2)} \left(\eta \sum_{i=1}^d H_i + 2\sqrt{1 - \beta_2} \sum_{i=1}^d \sigma_i + 2\tau \eta \sqrt{\sum_{i=1}^d H_i^2} \right) \max_i \mathbb{E} \ln \frac{v_{T,i} + \epsilon}{v_{0,i} + \epsilon} \\
 &\leq \frac{2}{\eta T} \mathbb{E}[f(x_0) - \min_x f(x)] + \eta \sum_{i=1}^d H_i + 2\sqrt{1 - \beta_2} \sum_{i=1}^d \sigma_i + 2\tau \eta \sqrt{\sum_{i=1}^d H_i^2} \\
 &\quad + \frac{\beta_2}{T(1 - \beta_2)} \left(\eta \sum_{i=1}^d H_i + 2\sqrt{1 - \beta_2} \sum_{i=1}^d \sigma_i + 2\tau \eta \sqrt{\sum_{i=1}^d H_i^2} \right) \ln \frac{\mathbb{E} \max_i v_{T,i} + \epsilon}{v_0 + \epsilon} \\
 &\leq \frac{2}{\eta T} \mathbb{E}[f(x_0) - \min_x f(x)] + \eta(1 + 2\tau) \sum_{i=1}^d H_i + 2\sqrt{1 - \beta_2} \sum_{i=1}^d \sigma_i \\
 &\quad + \frac{\beta_2}{T(1 - \beta_2)} \left(\eta(1 + 2\tau) \sum_{i=1}^d H_i + 2\sqrt{1 - \beta_2} \sum_{i=1}^d \sigma_i \right) \ln \frac{\mathbb{E} \max_i v_{T,i} + \epsilon}{v_0 + \epsilon}.
 \end{aligned}$$

We have used $\sqrt{\sum_{i=1}^d H_i^2} \leq \sum_{i=1}^d H_i$ for the final inequality.

From Lemma C.5, we define

$$E = \frac{2}{\eta T} \mathbb{E}[f(x_0) - \min_x f(x)] + \eta(1+2\tau) \sum_{i=1}^d H_i + 2\sqrt{1-\beta_2} \sum_{i=1}^d \sigma_i \\ + \frac{\beta_2}{T(1-\beta_2)} \left(\eta(1+2\tau) \sum_{i=1}^d H_i + 2\sqrt{1-\beta_2} \sum_{i=1}^d \sigma_i \right) F$$

where

$$F = 2 \ln \left(1 + \frac{\sum_{i=1}^d \sigma_i^2 + \|\nabla f(x_0)\|_\infty^2 + \sum_{i=1}^d H_i^2 \eta^2 T \left(T + \frac{1}{1-\beta_2} \right)}{v_0 + \epsilon} \right) + \ln 32.$$

Then,

$$\frac{1}{T} \mathbb{E} \left[\sum_{i=1}^d \sum_{t=1}^T \frac{\bar{g}_{t,i}^2}{\sqrt{\tilde{v}_{t,i} + \epsilon}} \right] \leq E.$$

By Lemma C.4 and Cauchy-Schwarz inequality,

$$\frac{2}{T} \mathbb{E} \sum_{t=\frac{T}{2}+1}^T \sum_{i=1}^d |\bar{g}_{t,i}| \leq \left(\frac{2}{T} \sum_{t=\frac{T}{2}+1}^T \sum_{i=1}^d \frac{\bar{g}_{t,i}^2}{\sqrt{\tilde{v}_{t,i} + \epsilon}} \right)^{1/2} \left(\frac{2}{T} \mathbb{E} \sum_{t=\frac{T}{2}+1}^T \sum_{i=1}^d \sqrt{\tilde{v}_{t,i} + \epsilon} \right)^{1/2} \\ \leq \sqrt{2E} \left(4E + \frac{4\beta_2^{T/4}}{T(1-\beta_2)} d\sqrt{v_0} + \sum_{i=1}^d \sigma_i + d\sqrt{\epsilon} \right)^{1/2} \\ \leq 2\sqrt{2E} + \sqrt{2}\sqrt{E} \sqrt{\frac{4\beta_2^{T/4}}{T(1-\beta_2)} d\sqrt{v_0} + \sum_{i=1}^d \sigma_i + d\sqrt{\epsilon}}.$$

Finally, the following holds:

$$\min_{\frac{T}{2} < t \leq T} \mathbb{E}[\|\nabla f(x_t)\|_1] \leq \frac{1}{T} \sum_{t=\frac{T}{2}+1}^T \sum_{i=1}^d |\bar{g}_{t,i}| \leq \mathcal{O} \left(E + \sqrt{E} \sqrt{\frac{\beta_2^{T/4}}{T(1-\beta_2)} d\sqrt{v_0} + \sum_{i=1}^d \sigma_i + d\sqrt{\epsilon}} \right)$$

with

$$E = \frac{2}{\eta T} \mathbb{E}[f(x_0) - f(x_{T+\tau})] + \left(1 + \frac{\beta_2 F}{T(1-\beta_2)} \right) \left(\eta \sum_{i=1}^d H_i + 2\sqrt{1-\beta_2} \sum_{i=1}^d \sigma_i + 2\tau\eta \sqrt{\sum_{i=1}^d H_i^2} \right)$$

and

$$F = 2 \ln \left(1 + \frac{\sum_{i=1}^d \sigma_i^2 + \|\nabla f(x_0)\|_\infty^2 + \sum_{i=1}^d H_i^2 \eta^2 T \left(T + \frac{1}{1-\beta_2} \right)}{v_0 + \epsilon} \right) + \ln 32.$$

When we assume $v_0 + \epsilon > \left(\sum_{i=1}^d \sigma_i^2 + \|\nabla f(x_0)\|_\infty^2 + \sum_{i=1}^d H_i^2 \eta^2 \right) / \text{poly}(T)$ and $\frac{1}{1-\beta_2} = \text{poly}(T)$, then $F = \mathcal{O}(\log T)$. Terms involving $\sum_{i=1}^d \sigma_i$ have a lower bound $\Theta \left(\sum_{i=1}^d \sigma_i \left(\frac{\log T}{T} \right)^{1/2} \right)$ with $1-\beta_2 = \Theta \left(\frac{\log T}{T} \right)$. Terms involving η has a lower bound $\Theta \left(\sqrt{\frac{(f(x_0) - \min_x f(x))(1+\tau) \sum_{i=1}^d H_i}{T}} \right)$ reached by $\eta = \Theta \left(\sqrt{\frac{f(x_0) - \min_x f(x)}{T(1+\tau) \sum_{i=1}^d H_i}} \right)$.

For $R \triangleq (f(x_0) - \min_x f(x)) \sum_{i=1}^d H_i$, $\beta_1 = 0$, $1 - \beta_2 = \Theta\left(\frac{\log T}{T}\right)$, $\eta = \Theta\left(\sqrt{\frac{f(x_0) - \min_x f(x)}{T(1+\tau) \sum_{i=1}^d H_i}}\right)$, $v_0 + \epsilon > \left(\sum_{i=1}^d \sigma_i^2 + \|\nabla f(x_0)\|_\infty^2 + \sum_{i=1}^d H_i^2 \eta^2\right) / \text{poly}(T)$, and $\frac{1}{1-\beta_2} = \text{poly}(T)$, we have

$$\min_{\frac{T}{2} < t \leq T} \mathbb{E}\|\nabla f(x_t)\|_1 = \mathcal{O}\left(\sqrt{\frac{(1+\tau)R}{T}} + \sqrt{\sum_{i=1}^d \sigma_i} \left(\frac{(1+\tau)R}{T}\right)^{1/4} + \sum_{i=1}^d \sigma_i \left(\frac{\log T}{T}\right)^{1/4} + \delta_T\right)$$

with $\delta_T = \sqrt{\frac{dv_0}{T(1-\beta_2)}} \exp\left(-\frac{T(1-\beta_2)}{8}\right) \left[\left(\frac{(1+\tau)R}{T}\right)^{1/4} + \sqrt{\sum_{i=1}^d \sigma_i} \left(\frac{\log T}{T}\right)^{1/4}\right]$. \square

D. Proof of Basis Misalignment Analysis

In this section, we provide the proof of the Hessian approximation comparison in Section 3.2. Before we begin the proof, we present useful lemmas regarding the Kronecker product.

Lemma D.1. (*Henderson & Searle (1981)*) Let A, B, C be matrices of appropriate dimensions. Then the following holds:

$$\text{vec}(ABC) = (C^\top \otimes A) \text{vec}(B)$$

Lemma D.2. (*Horn & Johnson (1991)*) Let A, B, A', B' be matrices of appropriate dimensions. Then the followings hold:

1. $(A \otimes B)(A' \otimes B') = (AA') \otimes (BB')$
2. $(A \otimes B)^\top = (A^\top \otimes B^\top)$

Lemma D.3.

$$\|A \otimes B\|_{(1,1)} = \|A\|_{(1,1)} \|B\|_{(1,1)}$$

Proof. $\|A \otimes B\|_{(1,1)} = \sum_{i,j,k,l} |A_{ik} B_{jl}| = (\sum_{ik} |A_{ik}|) (\sum_{jl} |B_{jl}|) = \|A\|_{(1,1)} \|B\|_{(1,1)}$. \square

D.1. Proof of Theorem 3.1

Let us restate the theorem here for the sake of readability.

Theorem 3.1. Let U and V be the matrices whose columns are eigenvectors of $\mathbb{E}[GG^\top]$ and $\mathbb{E}[G^\top G]$ respectively. If Hessian admits a Kronecker-factorized empirical Fisher, the following inequalities hold:

$$\|H_{U,V}\|_{(1,1)} \leq \|H_U\|_{(1,1)} \leq \|H\|_{(1,1)}.$$

Moreover, $\|H_{U,V}\|_{(1,1)}$ achieves the global minimum over all rotations.

In this proof, we rely on the key property of the Hessian with exact Kronecker product form.

Lemma D.4. if $\mathbb{E}[gg^\top] = A \otimes B$ for some $A \in \mathbb{R}^{n \times n}$ and $B \in \mathbb{R}^{m \times m}$, then

$$\mathbb{E}[gg^\top] = c \cdot \mathbb{E}[G^\top G] \otimes \mathbb{E}[GG^\top]$$

for some scalar c .

Proof. By the definition of Kronecker product, $\forall i, j, k, l : \mathbb{E}[G_{ij}G_{kl}] = A_{jl}B_{ik}$ holds. Then each entry of the matrices $\mathbb{E}[GG^\top]$ and $\mathbb{E}[G^\top G]$ satisfies

$$\begin{aligned} (\mathbb{E}[GG^\top])_{ik} &= \sum_j \mathbb{E}[G_{ij}G_{kj}] = \sum_j A_{jj}B_{ik} = \text{Tr}(A) \cdot B_{ik} \\ (\mathbb{E}[G^\top G])_{jl} &= \sum_i \mathbb{E}[G_{ij}G_{il}] = \sum_i A_{jl}B_{ii} = A_{jl} \cdot \text{Tr}(B). \end{aligned}$$

Thus, $\mathbb{E}[GG^\top]$ and $\mathbb{E}[G^\top G]$ are scalar multiplications of B and A , respectively. \square

Now, we are ready to prove Theorem 3.1.

Proof. Since Hessian admits a Kronecker factorized empirical Fisher, $H = \mathbb{E}[gg^\top] = A \otimes B$ holds with some $A \in \mathbb{R}^{n \times n}$ and $B \in \mathbb{R}^{m \times m}$. From Lemma D.4, and the definitions of U and V in the theorem, we can write the eigendecompositions as:

$$A = V\Lambda_A V^\top, \quad B = U\Lambda_B U^\top,$$

where Λ_A and Λ_B are diagonal matrices.

By Lemma D.1, rotated parameterizations corresponds to $\tilde{w} = (I \otimes U^\top)w$ and $\tilde{w} = (V^\top \otimes U^\top)w$.

Then Hessian in the rotated space is

$$H_U = (I \otimes U^\top)(A \otimes B)(I \otimes U) = A \otimes (U^\top BU) = A \otimes \Lambda_B, \quad (6)$$

$$H_{U,V} = (V^\top \otimes U^\top)(A \otimes B)(V \otimes U) = (V^\top AV) \otimes (U^\top BU) = \Lambda_A \otimes \Lambda_B, \quad (7)$$

where in the second equalities, we use Lemma D.2 and in the last equalities, we used Lemma D.4 in both (7) and (6). For any symmetric matrix, the $(1, 1)$ -norm is minimized when the matrix is diagonalized by its eigenbasis. Therefore:

$$\|\Lambda_A\|_{(1,1)} \leq \|A\|_{(1,1)} \quad \text{and} \quad \|\Lambda_B\|_{(1,1)} \leq \|B\|_{(1,1)}.$$

Thus, Lemma D.3 concludes the theorem. \square

D.2. Basis misalignment Analysis for $\mathcal{S} = 1^{\text{st}}$

Here, we present a result for the $\mathcal{S} = 1^{\text{st}}$ strategy analogous to Theorem 3.1, but under a different assumption regarding the Hessian's structure. Under the assumption $H = \mathbb{E}[g]\mathbb{E}[g]^\top$, we can show the following.

Theorem D.5. *Let orthogonal matrices U, V be $\mathbb{E}[G] = U\Sigma V^\top$. If Hessian has an exact Kronecker product form, the following inequalities hold:*

$$\|H_{U,V}\|_{(1,1)} \leq \|H_U\|_{(1,1)} \leq \|H\|_{(1,1)}.$$

Moreover, $\|H_{U,V}\|_{(1,1)}$ attains the global minimum over all orthogonal rotations.

However, in practice, $\mathbb{E}[g]\mathbb{E}[g]^\top$ is not guaranteed to be a faithful approximation of the true Hessian. This discrepancy potentially limits the approximation fidelity and, consequently, the optimizer's robustness to gradient delay in empirical settings.

Proof. Recall that $H = \mathbb{E}[g]\mathbb{E}[g]^\top$. The rotated Hessians are defined as:

$$H_U = (I \otimes U^\top)\mathbb{E}[g]((I \otimes U^\top)\mathbb{E}[g])^\top, \quad (8)$$

$$H_{U,V} = (V^\top \otimes U^\top)\mathbb{E}[g]((V^\top \otimes U^\top)\mathbb{E}[g])^\top. \quad (9)$$

For any rank-1 matrix $M = zz^\top$, $(1, 1)$ -norm satisfies $\|M\|_{(1,1)} = \|zz^\top\|_{(1,1)} = \|z\|_1^2$. By Lemma D.1, $(I \otimes U^\top)\mathbb{E}[g] = \text{vec}(\Sigma V^\top)$, $(V^\top \otimes U^\top)\mathbb{E}[g] = \text{vec}(\Sigma)$ holds. Thus, proving the theorem is equivalent to showing $\|\Sigma\|_{(1,1)} \leq \|\Sigma V^\top\|_{(1,1)} \leq \|U\Sigma V^\top\|_{(1,1)}$.

Since H is rank-1 and we assume it admits an exact Kronecker product structure, $\mathbb{E}[G]$ must also be rank-1. Let $\mathbb{E}[G] = \sigma_1 u_1 v_1^\top$, where u_1 and v_1 are the first columns of U and V , respectively, and σ_1 is the singular value.

Since U and V are orthogonal, $\|u_1\|_2 = \|v_1\|_2 = 1$. By the norm inequality $\|x\|_1 \geq \|x\|_2$, we have $\|u_1\|_1 \geq 1$ and $\|v_1\|_1 \geq 1$. Therefore, the following inequalities hold:

$$\begin{aligned} \|\Sigma\|_{(1,1)} &= \sigma_1 \\ &\leq \sigma_1 \|v_1\|_1 = \|\Sigma V^\top\|_{(1,1)} \\ &\leq \sigma_1 \|v_1\|_1 \|u_1\|_1 = \|u_1 \sigma_1 v_1^\top\|_{(1,1)} = \|U\Sigma V^\top\|_{(1,1)}. \end{aligned}$$

This implies $\|H_{U,V}\|_{(1,1)} \leq \|H_U\|_{(1,1)} \leq \|H\|_{(1,1)}$. Furthermore, the diagonal form $\|H_{U,V}\|_{(1,1)}$ attains the global minimum. \square

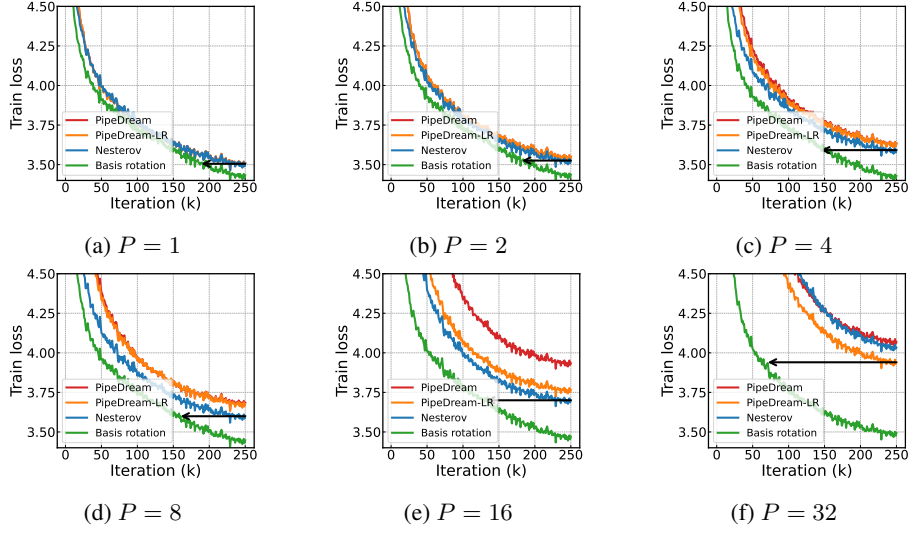


Figure 11. Comparison of each method for different number of stages P . The gap between basis rotation and baselines increases with larger P .

E. Connection to Recent Optimizers

In this section, we establish a connection between the design axes of eigenbasis-estimation and existing modern optimizers to contextualize our framework within the current literature. While our methodology shares conceptual roots with several recent optimizers, we introduce eigenbasis-estimation as a unified abstraction designed to isolate the effects of Hessian geometry from other implementation variables, such as momentum accumulation space or the use of power iteration instead of exact Singular Value Decomposition (SVD).

Our 2nd strategy is closely related to SOAP (Vyas et al., 2025) and EShampoo (Eschenhagen et al., 2025). However, a key technical distinction lies in the accumulation space of the optimizer states and the timing of the basis update. Unlike the official implementation of SOAP, which accumulates the first momentum in a rotated space and updates the eigenbasis after the parameter update step, our 2nd approach accumulates the first momentum in the original space and refreshes the basis before the optimization step. While accumulation in the rotated space requires projecting the momentum back and forth between bases during updates, accumulation in the original space does not require this additional computation. Furthermore, while EShampoo relies on SVD to compute eigenvectors, our implementation uses a single step of power iteration and QR decomposition to approximate them.

Similarly, our 1st strategy shares commonalities with GaLore (Zhao et al., 2024), LDAdam (Robert et al., 2025) (for unilateral), and the SVD-rotated AdamW variant discussed in Zhang et al. (2025a) (for bilateral). The primary departure from these methods is our use of the momentum matrix M_t as the source for basis estimation, whereas GaLore and AdamW-SVD typically derive their rotation matrices from the instantaneous, noisy gradient G_t . Furthermore, unlike GaLore and AdamW-SVD—which accumulate momentum in a rotated space and rely on exact SVD—our approach maintains accumulation in the original space and utilizes power iteration. Finally, because eigenbasis-estimation remains strictly full-rank, it avoids the complex error-buffer mechanisms found in LDAdam.

By standardizing the optimizer’s internal mechanics, we can systematically analyze how different basis estimation strategies interact with the loss landscape and gradient delay without being confounded by the implementation details of individual optimizers.

F. More Experimental Results

Full Results of Section 4.2 We plot the full results of Figure 5 in Figures 11 to 13. As seen in Figure 11, the gap between basis rotation and baselines becomes larger with increasing number of stages P . We also find that the slowdown, defined as the iteration ratio required to reach target loss for $P = 32$ relative to $P = 1$, becomes significantly smaller for basis rotation (see Figure 12). We note that this slowdown becomes smaller with more accurate eigenbasis-estimation strategies.

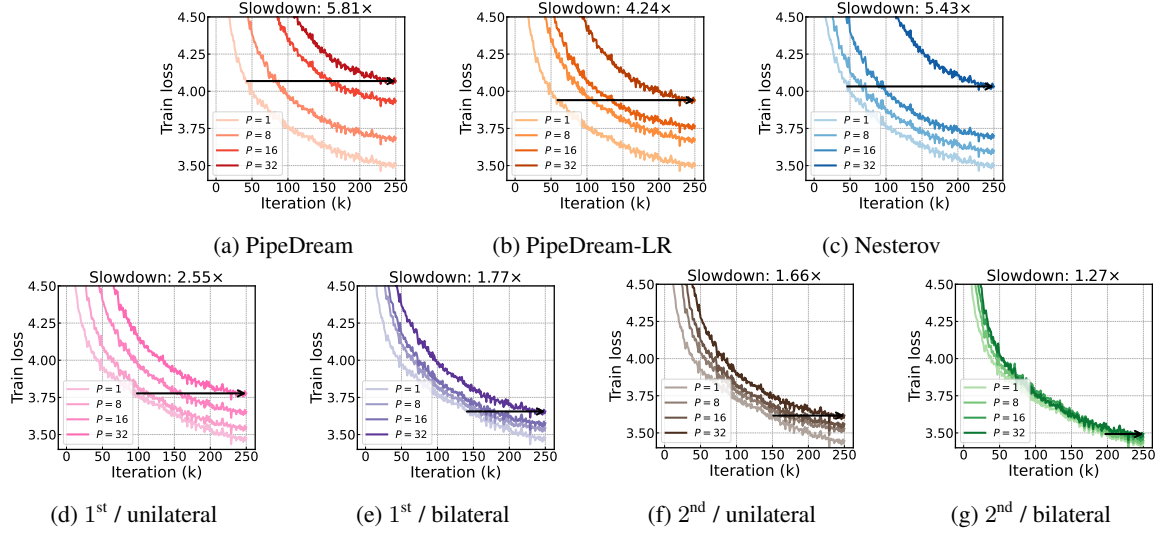


Figure 12. Slowdown for different methods when increasing the number of stages P for baselines (a-c) and basis rotation (d-g). Here, slowdown is defined as the iteration ratio required to reach target loss for $P = 32$ relative to $P = 1$.

Finally, we plot the full results of Figure 6 in Figure 13 where we increase the number of stages by increasing the number of Transformer blocks. While baseline methods invalidate the standard scaling law with increasing loss for larger models, basis rotation, especially with high-fidelity eigenbasis-estimation strategies, recovers the scaling law by gradually decreasing the loss for larger models.

Full Results of Section 4.3 We plot the full results of Figure 8 in Figure 14. We note that the high-fidelity estimation strategy consistently outperforms its memory-efficient counterpart across all number of stages, with a widening gap for larger stages. We also note that even the least accurate estimation strategy (1st/unilateral) consistently outperforms the best-performing baseline with a widening gap for larger stages.

Results for Validation Loss We also plot the validation loss in Figure 15. Here, we measure validation loss for 200 examples every 1000 iteration. We observe that the trend is very similar to the results for train loss.

Experiments for Other Baselines We also compare our approach against Delay Compensation (DC) algorithm (Zheng et al., 2017). This was originally proposed for asynchronous data parallelism and later adapted to pipeline parallelism for small-scale vision models (Jang et al., 2023). Specifically, DC uses a first-order Taylor expansion to approximate the fresh gradient $\nabla f(w_t)$ from the delayed gradient $\nabla f(w_{t-\tau})$:

$$\nabla f(w_t) \approx \nabla f(w_{t-\tau}) + \lambda \nabla f(w_{t-\tau}) \odot \nabla f(w_{t-\tau})(w_t - w_{t-\tau}),$$

where $\lambda \in [0, 1]$ is a hyperparameter to control the scale the compensation term and the diagonal empirical Fisher $\nabla f(w_{t-\tau}) \odot \nabla f(w_{t-\tau})$ serves as a diagonal approximation of the Hessian. We test $\lambda \in \{0.04, 0.1, 0.5, 1.0\}$.

The results are plotted in Figure 16. We observe that DC does not effectively address delayed gradients for large delays and shows similar performance to PipeDream.

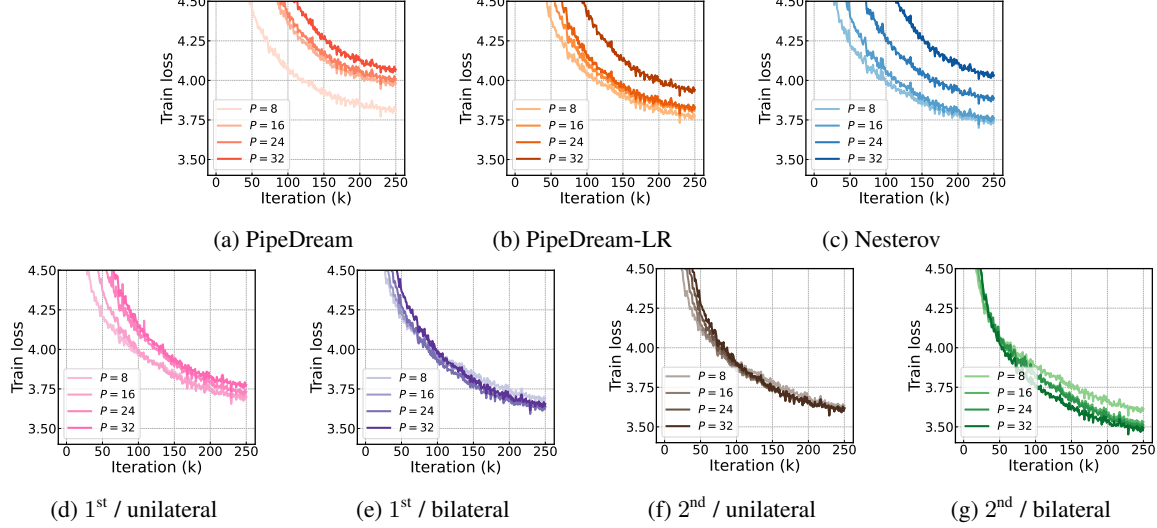


Figure 13. Performance of each method when increasing the number of stages by scaling the number of blocks for baselines (a-c) and basis rotation (d-g). While scaling the model rather increases the loss under asynchronous pipeline parallelism for baselines (a-c), scaling works well for basis rotation especially for 2nd/bilateral strategy (f).

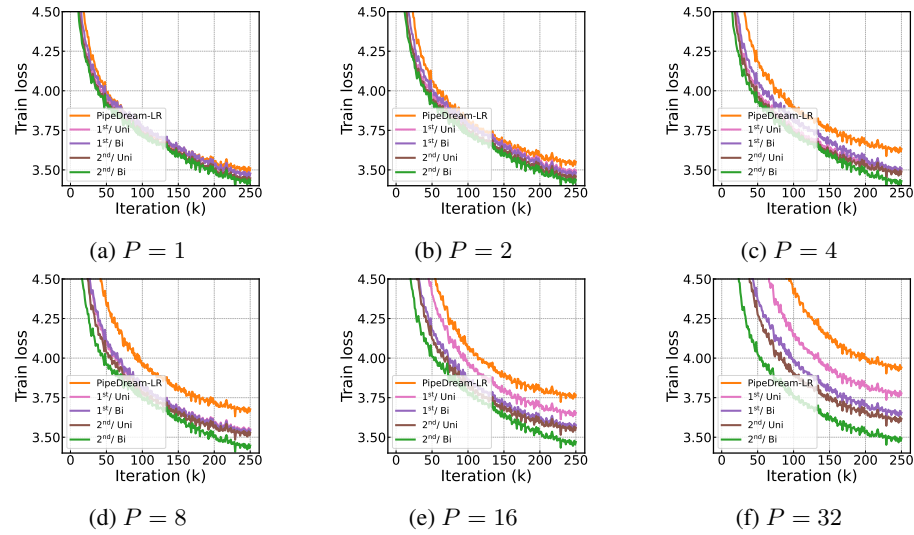


Figure 14. Comparison of different eigenbasis-estimation strategies for different number of stages P .

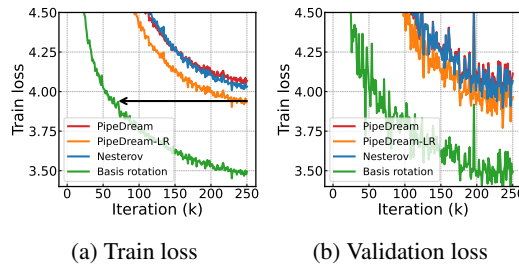


Figure 15. Train loss (a) and validation loss (b) for different methods at $P = 32$. The trend in validation loss closely follows the trend in train loss.

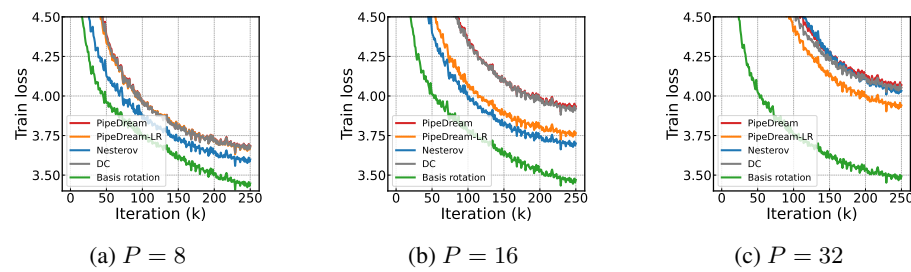


Figure 16. Comparison of each method for different number of stages P including Delay Compensation (DC) algorithm (Zheng et al., 2017) as baselines. DC shows similar performance to PipeDream.